Sedimentology and U-Pb dating of Carboniferous to Permian continental series of the northern Massif Central (France): Local palaeogeographic evolution and larger scale correlations

Céline Ducassou, Mathilde Mercuzot, Sylvie Bourquin, Camille Rossignol, P. Pellenard, L. Beccaletto, Marc Poujol, Erwan Hallot, Anne-Catherine Pierson-Wickmann, Charline Hue, et al.

Accepted Manuscript

Sedimentology and U-Pb dating of Carboniferous to Permian continental series of the northern Massif Central (France): Local palaeogeographic evolution and larger scale correlations

C. Ducassou, M. Mercuzot, S. Bourquin, C. Rossignol, L. Beccaletto, P. Pellenard, M. Poujol, E. Hallot, A.C. Pierson-Wickmann, C. Hue, E. Ravier
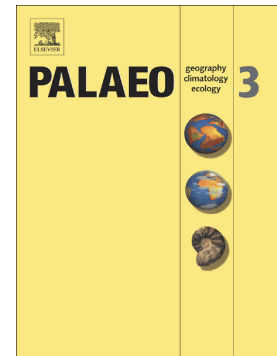
Please cite this article as: C. Ducassou, M. Mercuzot, S. Bourquin, et al., Sedimentology and U-Pb dating of Carboniferous to Permian continental series of the northern Massif Central (France): Local palaeogeographic evolution and larger scale correlations, Palaeogeography, Palaeoclimatology, Palaeoecology, https://doi.org/10.1016/j.palaeo.2019.06.001

Sedimentology and U-Pb dating of Carboniferous to Permian continental series of the northern Massif Central (France): local palaeogeographic evolution and larger scale correlations

Ducassou, C.[1], Mercuzot, M. [1], Bourquin, S. [1], Rossignol, C. [2], Beccaletto, L. [3], Pellenard, P. [4], Poujol, M. [1], Hallot, E. [1], Pierson-Wickmann, A.C. [1], Hue, C. [1], Ravier, E. [5]

[1] Univ Rennes, CNRS, Géosciences Rennes - UMR 6118, F-35000, Rennes, France

[2] Universidade de São Paulo, Departamento de Geofísica, Instituto de Astronomia, Geofísica e Ciências Atmosféricas, Rua do Matão, 1226-Cidade Universitária, Butantã, 05508-090 São Paulo, SP, Brazil

[3] Biogéosciences UMR uB/CNRS 6282, Université Bourgogne Franche-Comté, 21000 Dijon, France

[4] Bureau de Recherche Géologique et Minière, 3 Avenue Claude Guillemin, 45100 Orléans, France

[5] Laboratoire de Planétologie et Géodynamique, UMR 6112, CNRS, Le Mans Université, Avenue Olivier Messiaen, 72085 Le Mans CEDEX 9, France

Corresponding author: Ducassou, C. (celine.ducassou@gmail.com)

Abstract:

The Carboniferous to Permian volcanic-sedimentary succession shown by the LY-F core from the Lucenay-lès-Aix area, in the northern part of the Massif Central, has been studied in order to obtain both landscape reconstructions (sedimentological analyses) and geochronological constraints (U-Pb dating on zircon and apatite). The lowermost part

of the core consists mainly of lacustrine deposits with Gilbert-type delta and volcaniclastic-rich fan delta deposits including several altered volcanic ash layers (tonstein). In contrast, in the uppermost part of the core, playa-lake deposits dominate. LA-ICP-MS U-Pb analyses were performed on both zircon and apatite grains from interbedded tonsteins. This coupled U-Pb dating approach allows to assess potential reworking of volcanic material or the occurrence of non-volcanic grains, such as xenocrysts, in order to provide better evaluations for the depositional ages of the tonsteins. These investigations reveal that sedimentation took place between the late Gzhelian and the late Sakmarian (i.e., between c. 301 and 290 Ma). This sedimentary succession can therefore be compared to those from adjacent basins for which geochronological constraints are available (i.e., Autun and Lodève basins, resp. located north and south of the Massif Central). This study provides a reference section for future comparisons with similar sections from other Carboniferous to Permian basins, in France as well as elsewhere in Europe.

Keywords : Depositional environment; Sequence stratigraphy; Tonstein; U-Pb; Zircon; Apatite

Highlights :

- The LY-F section contains lacustrine deposits with interbedded tonstein layers.

- The lower part of the core consists of Gilbert-type deltas deposits.

- They are interbedded with volcaniclast-rich delta deposits.

- The upper part of the core consists of playa-lake deposits.

- The depositional age of the LY-F section is late Gzhelian to late Sakmarian.

1. Introduction

In Europe, the Carboniferous to Permian transition is marked by the final stages of the Variscan orogeny that resulted from the assembly of several continents to form Pangea. This period is not only a time of tectonic changes, but also of major climatic disruption, with the transition from icehouse to greenhouse conditions (i.e., Beerling et al. 2002; Scheffler et al. 2003). This climatic change is marked by an increase in atmospheric pCO$_2$ (Montañez et al., 2007; Poulsen et al., 2007), as well as by an aridification over most of equatorial Pangea during the early Permian (Schneider et al., 2006; Tabor and Poulsen, 2008; Tabor et al., 2013; Gulbranson et al., 2015; Michel et al., 2015). In the European continental basins, the preserved palaeoflora suggest that the climate became warm and semi-arid (Schneider et al., 2006). However, Pochat and Van Den Driessche (2011) have highlighted that some of the observations attributed to this climate change, such as the palaeo-environmental change from deep to shallow lakes, could instead be ascribed to the syn-rift tectonic evolution of the basins. Moreover, the sedimentary record of the Carboniferous to Permian transition in western Europe is limited to small intracontinental basins, for which the stratigraphic framework is often poorly constrained. The terminology used to refer to the stratigraphic record of these basins only reflect lithostratigraphic units with specific floristic facies (i.e., Stephanian, Autunian, Saxonian and Thuringian), by definition diachronous both in time and space (Broutin et al., 1986; 1999), but sometimes attributed to regional continental stages (e.g., Heckel and Clayton, 2006; Menning et al., 2006; Schneider et al., 2017). Correlating these units to the International Carboniferous to Permian Stratigraphic Chart is therefore challenging. The acquisition of isotopic ages from interbedded volcanic ash layers have provided a chronostratigraphic framework for several basins in France (Bruguier et al.,

2003, for the south of the Massif Central, and more specifically: Michel et al., 2015 for the Lodève Basin; Pellenard et al., 2017 for the Autun Basin), and in the Czech Republic (Opluštil et al., 2016a, 2016b, 2017). However, chronostratigraphic data are still lacking for many other Carboniferous-Permian basins. The present study, based on the core from the Lucenay F well (LY-F) located in the Decize-La Machine area (Massif Central, France, Fig. 1), aims at re-evaluating the depositional environments of the sediments (facies analysis, petrographic analysis) to provide a model for landscape evolution, in order to better constrain the relationships between tectonics, climate and volcanism, in this area. This study also aims to propose a chronostratigraphic framework for the interbedded volcanic ash layers based on LA-ICP-MS U-Pb analyses performed on both zircon and apatite. This new methodological approach was implemented to better evaluate the depositional ages of the volcanic ashes. Indeed, in the literature, depositional ages are usually determined from zircon U-Pb dating alone despite the fact that volcanic ashes may contain zircon grains that crystallized much before eruptions (inherited grains, xenocrysts, antecrysts, e.g. Rossignol et al. 2019, and references therein), and thus may yield dates that are older than the actual depositional ages. Conversely, older dates obtained from apatite crystals exotic to the magma are not expected to be preserved because of the low closure temperatures of this mineral (450-550°C, Schoene and Bowring, 2007). Apatite is therefore considered as suitable to provide additional constraints on depositional ages. Finally, our model is compared with the sedimentary record from other Carboniferous–Permian basins in the northern and southern Massif Central (France).

2. Geological setting

2.1. The Variscan orogeny

5

The Variscan orogeny, whose remains are preserved over much of western and central Europe, resulted from the collision of several peri-Gondwanan microcontinents that were located between two main colliding supercontinents, Laurussia and Gondwana (e.g., McCann, 2008). The precise geodynamic scenario is, however, still a matter of debate, especially when it comes to the nature, boundaries and timing of amalgamation of the peri-Gondwanan continental domains (e.g., Robardet, 2003; Ballèvre et al., 2014; Franke et al., 2017). In the Massif Central and the southern part of the Armorican Massif, in France (Fig. 1a), continental subduction resulted in the formation of HP-LT metamorphic rocks during the Late Devonian–early Carboniferous (Bosse et al., 2000; Paquette et al., 2017; Lotout et al., 2018). Subsequent nappe-stacking was accompanied by the progressive exhumation of HP-LT metamorphic rocks (Bosse et al., 2000; Pitra et al., 2010; Ducassou et al., 2014), during the early Carboniferous. Next, between the late Carboniferous and the early Permian, post-orogenic extension is recorded by the formation of high-grade metamorphic domes associated with detachment faults, such as the Velay (Ledru et al., 2001) or the Montagne Noire (Van Den Driessche and Brun, 1991; Poujol et al., 2017) domes in the Massif Central, the Lesponne and Chiroulet domes in the Pyrenees (Lemirre et al., 2019) or in the Quiberon and Sarzeau areas (Gapais et al., 2015), in the Armorican Massif. This extensive event is often attributed to the post-orogenic collapse of a thickened and hot crust (Ménard and Molnar, 1988; Echtler and Malavieille, 1990). In this geodynamic framework, late Carboniferous-Permian sedimentation is thought to occur in intramontane coal-basins, usually interpreted as half-grabens associated with major detachment faults (Malavieille et al., 1990; Van Den Driessche and Brun, 1991; Malavieille, 1993; Faure, 1995), or as pull-apart basins by reactivation of major shear zones (Vallé et al., 1988; Genna et al., 1998; Choulet et al., 2012).

2.2. Late Carboniferous-Permian basins

In France, the late Carboniferous–Permian (i.e., Stephanian–Autunian) basins are exposed within the Variscan basement from the Massif Central, Vosges, Armorican Massif, Pyrenees and Alps (Fig. 1a). They are also known from subsurface data beneath the Meso–Cenozoic sedimentary cover of the Paris, Aquitaine and South-East basins (see Beccaletto et al., 2015 and references therein).
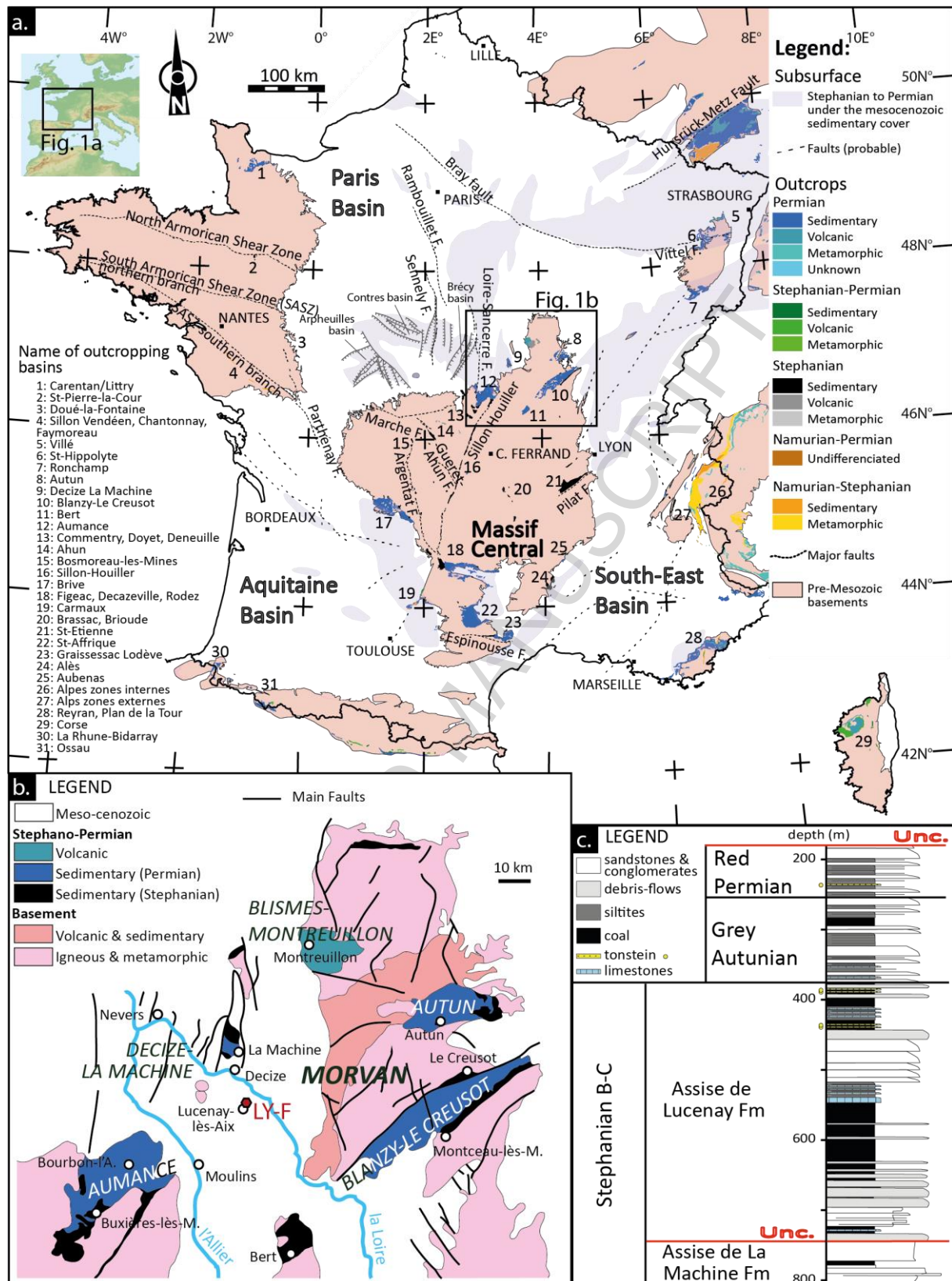
Fig. 1 a) Simplified geological map of France showing the location of the Stephanian

and Permian deposits (surface data: Chantraine et al. 2003; subsurface data: Debrand-

Passard et al., 1984; Châteauneuf and Farjanel, 1989; Delmas et al., 2002; Beccaletto et al.,

8

2015); b) Simplified geological map and basins location for the northeastern part of the Massif Central (modified after Gand et al., 2007). The location of the LY-F borehole is indicated on the map; c) Lithostratigraphic section of the Lucenay-lès-Aix area (modified from Donsimoni, 1990). Unc.: Unconformity.

In the northeastern part of the Massif Central, several of these Stephanian to Permian basins are preserved. From west to east, they are (Fig. 1b): (i) the Aumance (or Bourbon-l'Archambault) Basin, located between the Loire-Sancerre and the Sillon Houiller faults (Paquette, 1980; Bonnion et al., 1983; Courel et al., 1989; Paquette and Feys, 1989); (ii) the Decize-La Machine horst that is surrounded by a Mesozoic sedimentary cover, but which may represent a prolongation of the Aumance Basin (Grangeon et al., 1968); (iii) the Autun Basin, located in the Morvan and bounded to the south by the Autun fault (Marteau, 1983; Marteau and Feys, 1989); (iv) the Blanzy-Bert-Le Creusot-Burgondy Basin, extending over several hundred km from the Sillon Houiller to the south-west, up to the Vosges Mountains and the Forêt-Noire to the north-east (Feys and Gand, 1983; Vallé, 1986; Vallé et al., 1988; Gand, 2003). In addition, in the Morvan, the Blismes–Montreuillon volcanic units include rhyolitic lava flows, ignimbritic and tuff layers, and minor interbedded sediments. These units have been attributed to the Autunian from the flora content and have been dated as late Carboniferous to early Permian using fission tracks analyses on zircon (Carpéna et al., 1984). In the four Carboniferous to Permian basins, the sedimentary sequence has been divided into several lithostratigraphic units, named, from bottom to top: Stephanian (subdivided in Stephanian A, B and C), Autunian (itself subdivided in grey and red Autunian in the Aumance and Decize areas, or in Lower and Upper Autunian in the Autun Basin, e.g., Grangeon et al., 1968; Paquette, 1980; Marteau, 1983), and Saxonian. However, these

9

units, defined from their paleobotanical assemblages (Broutin et al., 1986, 1999), should not be directly related to the official stratigraphic periods as they may encompass the Carboniferous-Permian boundary, as shown in the Autun Basin, where the Carboniferous–Permian boundary has recently been established within the Lower Autunian using new CA-ID-TIMS U-Pb ages (Pellenard et al., 2017). High-precision CA-ID-TIMS U-Pb zircon ages are also available for the Lodève basin successions (Michel et al. 2015), located in the southern part of the Massif Central (Fig. 1a).

2.3. Lucenay-lès-Aix area

The Carboniferous-Permian sedimentation from the Lucenay-lès-Aix area is only known from subsurface data acquired during the 1980s (Donsimoni, 1990; 2006). The available drilled cores have never reached the basement of the sedimentary units. However, in the Decize-La Machine horst, located only a few tens of kilometers to the north, the Carboniferous to Permian sediments, represented by conglomeratic deposits, are deposited unconformably over a crystalline basement (Grangeon et al., 1968). From bottom to top, the succession of the Lucenay-lès-Aix area has been ascribed to the Stephanian B-C, the Grey Autunian and the Red Permian (Donsimoni, 1990) (Fig. 1c). These divisions were mainly based on floral assemblages (Primey and Farjanel, 1988) and lithological considerations (Donsimoni, 1990). In addition, the Stephanian B-C is subdivided in two formations (Fm) separated by an angular unconformity. The La Machine Fm is mainly made of feldspathic sandstones, polygenic conglomerates and rare fine-grained sediments and coal layers. It is overlain by the Lucenay Fm that contains thick coal accumulations, which are interbedded with conglomerates, sandstones, claystones, rare carbonates with stromatolites and a few tonstein layers. The Grey Autunian is mainly composed of feldspathic sandstones interbedded with siltites and rare

10

coal layers. The colour of this unit evolves from grey-greenish at the base to brown-reddish towards the top. At last, the Red Permian is mainly made of reddish claystones and sandstones. Occurrence of tonstein layers is also mentioned in this unit. In the absence of preserved fauna or flora, this unit was attributed to the Red Saxonian, only based on facies analogies. These sedimentary series are usually attributed to alluvial/fluvial, swamp and minor lacustrine depositional environments (Primey and Farjanel, 1988; Donsimoni, 1990). They are assumed to be deposited in a half-graben controlled by a major NNE-striking syn-sedimentary fault located towards the NW (Donsimoni, 1990).

3. Methodology

3.1. Sedimentological analyses

The LY-F core (WGS84 coordinates: latitude: 46.71872301; longitude: 3.49736547) is 328.5 m long and was studied to establish a detailed sedimentological reference section at a 1:50 scale. Each sample number corresponds to the name of the core (LYF) followed by the depth, in meters, to which the sample has been collected. The facies have been described using a terminology modified from Miall (1996) and Postma (1990). The evolutions of both the depositional environment and the source of the sediments were defined and constrained by facies associations and thin section analyses. From this detailed sedimentological study, the recognition of progradational-retrogradational trends within this terrestrial context (e.g., Bourquin et al., 1998; 2009) is given by the vertical depositional environment profile (Fig. 2).

3.2. Identification of ash-fall vs volcanic-sedimentary deposits

11

Ashes deposited in swamp and lake environments are transformed during the early diagenesis in clay minerals or silicate minerals (e.g., zeolites), depending on the alkalinity and acidity of the depositional environment (Fisher and Schmincke, 1984). Following in situ alteration, volcanic ash-layers mostly form tonsteins in coal-bearing sequences; they are characterised by a high kaolinite content derived from the devitrification of glass shards, and sometimes by smectite or illite-smectite mixed-layers when smectite has been altered by an increase in temperature during burial diagenesis (Bohor and Triplehorn, 1993; Spears, 2012). It is therefore generally accepted that tonsteins result from the in-situ alteration of volcanic ashes, mostly as distal air-falls from violent eruptions involving a silica-rich magma (Triplehorn, 1990). However, considering that kaolinite also occurs in coal-bearing sequences as a result of normal sedimentary processes, some kaolinite-rich layers may also correspond to detrital shales. Moreover, ash-fall deposits may be reworked during sedimentation and/or may incorporate detrital grains by various mechanisms (e.g., aeolian or aqueous contamination by currents, bioturbation...). Therefore, careful examinations of the mineralogical contents and geochemical compositions of the clay horizons is necessary to testify their pyroclastic nature, before using the zircon and/or apatite grains to date their deposition. In the case of the LY-F core, the temperature reached during burial diagenesis, as reported by Donsimoni (1990) based on the vitrinite reflectance index, has transformed smectite, which is very sensitive to a temperature increase, into R1-type illite-smectite mixed-layer (IS R1), while kaolinite, which is more heat resistant (up to 120-140°C), has been preserved. Therefore, kaolinite and IS R1 are considered as authigenic clay minerals formed from glassy ash shard deposits that likely correspond to tuffs, as frequently observed for tonsteins and K-bentonites (Spears, 2012; Huff, 2016; Hong et al., 2019). By contrast, mixtures of mica-illite, chlorite, kaolinite, vermiculite and associated mixed-layers (illite-smectite, chlorite-

12

vermiculite, smectite-vermiculite, chlorite-smectite) are common in deposits enclosing mostly detrital particles. Moreover, quartz and alkali feldspar (sanidine) are often observed in tonsteins derived from a felsic magmatism but high contents in these minerals may also reflect contamination by detrital input during reworking, which is frequent in continental or shallow water environment (Spears, 2012).

Fig. 2 Sedimentological log of the LY-F core (Lucenay F well) at the 1/50 scale. Facies codes (described in Table 2) are indicated in blue, to the left of each column. The depositional profile is based on the depositional environments obtained for each facies

14

association (see Table 3 and discussion in the text). The location of samples selected for thin sections, XRD and geochronological analyses are also reported.

3.2.1. XRD analyses

X-ray Diffraction (XRD) for the bulk rock and the clay-size fraction (< 2 μm) were performed at the Biogéosciences Laboratory (Université de Bourgogne) to determine the mineralogical content of 33 clay layers that potentially correspond to tonsteins, and 3 samples of the enclosing detrital sediments (Table 1). By comparison, the mineralogical contents of the layers distinguish tonsteins that are directly derived from volcanic ashes from volcanic-sedimentary rocks, containing a mixture of ashes and detrital particles (Pellenard et al. 2017; Rossignol et al., 2019).

Clay minerals were identified in oriented mounts of non-calcareous clay-size fraction, following the analytical procedure of Moore and Reynolds (1997). After removing carbonate using 0.2 N HCl, clays were deflocculated by successive rinsings with deionized water. Particles <2 μm were isolated after decantation (105 min) and concentrated by centrifugation. Diffractograms were obtained using a Bruker D4 Endeavor diffractometer with CuK_{α} radiation, LynxEye detector and Ni filter, under 40 kV voltage and 25 mA intensity. The goniometer scanned from 2.5° to 28.5° 2θ for each run. Mineral identifications and semi-quantitative estimates were based on the position and area of the (001) basal reflections on the three XRD diffractograms, obtained after air-drying (AD), ethylene-glycol solvation (EG), and heating at 490°C for 2 hours (Moore and Reynolds, 1997).

Samples	Bulk mineralogy (XRD powder, by order of content)		Kaol	IS R1	Illite	CV	Quartz
	very abundant >30% +, abundant, >15% (present >2%)		(%)	(%)	(%)	(%)	(%)
LYF325.3 [nv]	*Quartz+, IS R1/illite, kaolinite/chlorite (K feldspar, gypsum, plagioclase)*		*27*	*30*	*38*	*6*	*15*
LYF337.35	Quartz+ (dolomite, kaolinite, IS R1, mica/illite, goethite)		47	53	0	0	11
LYF363.35	**Dolomite +, kaolinite, siderite (gypsum, quartz, goethite)**		**93**	**7**	**0**	**0**	**3**
LYF367.15	* ‡	**Kaolinite+ (goethite, quartz)**	**100**	**0**	**0**	**0**	**1**
LYF386.88	IS R1, quartz, kaolinite (goethite, gypsum)		33	63	4	0	5
LYF416.5	* ‡	**Kaolinite+, goethite (gypse, quartz, IS R1)**	**88**	**12**	**0**	**0**	**0**
LYF448.08	‡	Quartz+, kaolinite+ (goethite, IS R1)	67	22	8	3	21
LYF464.7	Siderite+, quartz, kaolinite (K feldspar, mica/illite)		71	21	7	0	5
LYF470.53	Quartz+ (kaolinite, mica/illite, K feldspar, plagioclase)		36	38	22	4	27
LYF471.05 [nv]	*Quartz+ (IS R1/illite, goethite, kaolinite/chlorite)*		*10*	*47*	*41*	*1*	*60*
LYF473.25	* ‡	**Quartz+, kaolinite (goethite, IS R1)**	**68**	**32**	**0**	**0**	**18**
LYF481.95	*	**Kaolinite+, quartz+, goethite**	**94**	**6**	**0**	**0**	**7**
LYF482.15	* ‡	**Quartz+, goethite, kaolinite (K feldspar)**	**96**	**4**	**0**	**0**	**5**
LYF487.25	Kaolinite+, quartz+ (goethite, IS R1)		86	12	2	0	6
LYF488.15	Quartz+, kaolinite+ (goethite, mica/illite, IS R1)		75	14	11	0	9
LYF488.97	**Quartz+, kaolinite (goethite, plagioclase, IS R1)**		**70**	**29**	**0**	**1**	**27**
LYF491.25	* ‡	**Quartz+, kaolinite (IS R1, plagioclase, goethite)**	**58**	**42**	**0**	**1**	**24**
LYF492.7	Quartz+ (kaolinite, goethite)		73	21	5	1	80
LYF494.15	Kaolinite+, quartz + (goethite, mica/illite)		88	7	4	1	2
LYF498.5	**Dolomite+ (quartz)**		**89**	**11**	**0**	**0**	**3**
LYF503.9	Kaolinite+, quartz+ (mica/illite)		87	8	5	0	7
LYF504.1	Kaolinite+, quartz+ (goethite)		92	6	3	0	14
LYF504.95	Kaolinite+, quartz+ (goethite, mica/illite)		93	5	2	0	6
LYF505.26	Quartz +, kaolinite+ (goethite, mica/illite)		83	10	6	2	3
LYF516	Quartz+, kaolinite (ISR1, mica/illite, goethite, K feldspar, plagioclase)		29	46	22	3	11
LYF517.1 [nv]	*Quartz+, IS R1/illite (kaolinite/chlorite, plagioclase, K feldspar)*		*15*	*37*	*44*	*5*	*20*
LYF521.6 [nv]	*Quartz+, IS R1/illite, kaolinite/chlorite (K feldspar)*		*23*	*40*	*34*	*3*	*17*
LYF554.34	*	Kaolinite+, quartz (goethite, gypsum)	99	0	1	0	2
LYF554.35 [e]	*Quartz+, IS R1/illite, kaolinite/chlorite (K felspar, gypsum, apatite)*		*32*	*30*	*36*	*2*	*15*
LYF564.95	*	**Kaolinite+, goethite, quartz (IS R1)**	**89**	**11**	**0**	**0**	**1**
LYF567.70	* ‡	**Kaolinite+, quartz+ (goethite, IS R1)**	**81**	**19**	**0**	**0**	**8**
LYF567.85 [e]	*Quartz+, kaolinite/chlorite (IS R1/illite, K feldspar)*		*63*	*20*	*16*	*1*	*31*
LYF579.35	Kaolinite+, quartz (goethite)		97	1	2	0	1
LYF579.4	*	**Kaolinite+, goethite (quartz, gypsum)**	**100**	**0**	**0**	**0**	**0**
LYF579.6	*	**Kaolinite+, quartz (goethite, IS R1)**	**79**	**21**	**0**	**0**	**2**
LYF579.65 [e]	*Quartz+, kaolinite/chlorite (IS R1/illite, gypsum, goethite, K feldspar)*		*51*	*20*	*24*	*4*	*12*

* sample selected for chemical analysis

‡ sample selected for geochronological analysis

pure tonstein

mixed tonstein with a low detrital input

mixed tonstein with a signifant detrital input

non volcanogenic samples [nv]

sediments surrounding the tonstein layers [e]

Tab. 1 Results of XRD analyses performed on 33 clayey layers considered as potential tonsteins and 3 enclosed sediments: bulk mineralogy (XRD powder) and clay mineral proportion based on semi-quantification (given with 5% uncertainties) according

to Moore and Reynolds (1997) for the clay fraction. %Quartz values are calculated using the 4.26 Å peak area compared with areas of main clay mineral peaks.

3.2.2. *Major and trace element geochemical analyses*

Concentrations of major and trace elements (44 chemical elements) were quantified by Inductively Coupled Plasma-Optical Emission Spectrometry (ICP-OES) and Inductively Coupled Plasma Mass Spectrometry (ICP-MS), respectively, on 11 potential tonstein samples at the SARM (CRPG-CNRS, Nancy, France). Geochemical analyses are provided in Supplementary material 1 and were used to compare the geochemical signature of the tonsteins with those from the Autun Basin (Pellenard et al. 2017), in order to characterise the nature of the magmatism and discuss the possible centres of the volcanic emissions. Analytical uncertainties and detection limits are provided in Supplementary material 2.

3.3. **U-Pb geochronology**

3.3.1. *Analytical methods*

Zircon and apatite grains were extracted from samples from the LY-F core, following a classical mineral separation procedure, and hand-picked under a binocular microscope to produce the most representative sampling, with the aim to avoid any sampling bias (e.g., Sláma and Košler, 2012 and references therein; Malusà et al. 2013). After embedding the grains in an epoxy resin, the pucks were polished down to reveal equatorial cross sections. Zircon and apatite grains were then imaged by cathodoluminescence (CL) before analysis by LA-ICP-MS in Géosciences Rennes. Detailed operating and instrumental conditions for U-Pb analyses on zircon and apatite can be found in Ballouard et al. (2015)

17

and Pochon et al. (2016) and summarised in Supplementary materials 3 and 4, respectively.

3.3.2. Data filtering and age calculations

For the U-Pb analyses on zircon, a two-step procedure has been applied to derive the age of the samples. The first step consists in filtering the data based on their probability of concordance, calculated using the "concordia" function in Isoplot/Ex 3.00 (Ludwig, 2012), by comparing the $^{206}Pb/^{238}U$ and $^{207}Pb/^{235}U$ ratios and including the decay constant errors (Ludwig, 1998; Nemchin and Cawood, 2005; Rossignol et al., 2016; Zimmermann et al., 2017). The cut-off level applied to filter the data was 10 % (Rossignol et al., 2016). Hereafter, concordant analyses refer to those exhibiting a probability of concordance ≥ 10 %.

For the second step, only concordant data were considered. As a slight Pb loss could still result in apparently concordant dates, as in the Tera-Wasserburg diagram, the Pb loss trend tends to be parallel to the concordia curve (e.g., Corfu, 2013), resolving whether the data represent truly concordant ages or apparently concordant dates requires a close inspection of each dataset. In cases where the data do not show evidence of Pb loss, with no significant spread along the concordia curve, the youngest cluster of at least 3 grains with dates overlapping at 2 σ (standard deviation), as proposed by Dickinson and Gehrels (2009), is used to calculate a weighted mean concordia age from multiple analyses. In cases where data spread along the concordia curve, the selection of data to calculate a weighted mean concordia date from multiple analyses is discussed in detail in the text, because such spreading could result from variable amounts of Pb loss, hence producing apparently concordant dates with no geological significance.

Additionally, we used the Tuff Zirc algorithm (Ludwig and Mundil, 2002), implemented as the "zircon age extractor" tool in Isoplot/Ex 3.00 (Ludwig, 2012). This algorithm was developed to minimise the effects of both inheritance and Pb loss, by isolating the largest cluster of analyses yielding a probability-of-fit greater than 0.05, and calculating the median age of this cluster. The uncertainties are asymmetric and provided within a 95 % confidence limit. The TuffZirc algorithm was applied to the concordant ages (i.e., obtained using the "concordia" function) and the results are compared with the weighted mean concordia dates calculated from multiple analyses.

For the U-Pb analyses on apatite, no filtering was applied to the data before age calculations. Two approaches were used to derive the age of the samples. The first approach was to calculate the lower intercept of the discordia passing through the analyses. In each diagram, the unforced discordia is displayed together with a discordia for which the upper intercept was anchored to an initial $^{207}Pb/^{206}Pb$ value of 0.855 ±0.001, calculated according to the single stage Pb evolution model of Stacey and Kramers (1975) for an age of 293 ± 15Ma. The second approach was to calculate a weighted-average date based on the ^{207}Pb-corrected dates. These dates are obtained using the data reduction scheme VizualAge_UcomPbine (Chew et al., 2014) with a fixed initial $^{207}Pb/^{206}Pb$ value of 0.855.

4. Sedimentological analyses and depositional environment evolution

From the sedimentological study performed on the LY-F core, 18 facies have been distinguished (Table 2): 10 conglomerate and sandstone facies, 4 fine-grained facies and 4 additional facies (including coal, volcanic ashes and carbonates). These facies have been grouped in 9 facies associations (Table 3) reflecting the depositional environments evolution along the LY-F section.

19

Code	Lithology	Sedimentary structures	Depositional process
Conglomerate and sandstone			
GSm	Rounded to angular coarse-grained sand to boulders Polygenetic clasts (quartz, feldspars, coal fragments), well-sorted to moderately sorted (Fig. 3a, f) Clast supported Bed thickness: dm to m	Massive Planar bed Ungraded, and sometimes inverse, inverse-to-normal or normal grading Erosive base Sometimes chaotic features	Masse freezing, cohesive debris flow deposits or high-density turbidity current (Davies and Walker, 1974; Walker, 1975; Lowe 1982; Postma, 1990; Postma et al., 2014) Some slump and slide occurrences
GSt	Same lithology than the GSm facies (Fig. 3a) Bed thickness: dm to m	Trough cross stratification Erosive base	Tractive current, 3D megaripple migration (Davies and Walker, 1974; Walker, 1975. Miall, 1978)
IGSm	Same lithology than the GSm facies (Fig. 3b) Bed thickness: dm to m	Massive Inclined bed from 15 to 25° Ungraded, and sometimes inverse, inverse-to-normal or normal grading Erosive base Sometimes chaotic features	Gravity process, debris flow deposits in active foreset (Davies and Walker, 1974; Walker, 1975; Postma, 1990; Postma et al., 2014) Some slump and slide occurrences
IGSt	Same lithology than the GSm facies Bed thickness: dm to m	Trough cross stratification Inclined bed from 15 to 25° Erosive base	Multistored hydraulic jump (Cartigny et al., 2014 ; Rubi et al., 2018)
GSh	Same lithology than the GSm facies Bed thickness: dm	Planar horizontal lamination Erosive base	Hyperconcentrated density flow, High density turbidity deposits (Walker, 1975; Postma, 1990; Mulder and Alexander, 2001)
Gmm 1	Rounded to angular gravel to boulders, Polygenetic clasts (mud-clasts, magmatic and coal fragments), very poorly sorted (Fig. 3c, 3h) Matrix supported, very poorly sorted (silt to coarse-grained sand) Bed thickness: dm to m	Massive Ungraded, and sometimes inverse, inverse-to-normal or normal grading Sharp base Sometimes chaotic features	Masse freezing, cohesive debris flow deposits (Walker, 1975; Lowe, 1982; Postma, 1990. Miall, 1996;) With some slump and slide occurrences
Gmm 2	Rounded to angular gravel to pebbles, Polygenetic clasts (mud-clasts, magmatic and coal fragments), poorly sorted, Matrix supported very poorly sorted (silt to coarse-grained sand) Bed thickness: dm	Massive Ungraded, and sometimes inverse, inverse-to-normal or normal grading Sharp base Sometimes chaotic and shearing features	High density turbidity current (Walker, 1975; Postma, 1990) With some slump and slide occurrences
GFd	Deformed bed of various lithology (conglomerate to silt, Fig. 3j, 3n) Bed thickness: dm to m	Chaotic deposits and shearing structures	Slump and slide

Smm	Heterolithic well-bedded very fine to coarse-grained sand with floating gravels to pebbles (Fig. 3l) Bed thickness: dm	Horizontal planar bedding Gravels to pebbles are sometimes inverse or inverse-to-normal grading, diffuse base and top between conglomerate and sand Sharp or diffuse base	Traction carpet, gravelly high density turbidity deposits (Lowe, 1982)
Sl	Fine to medium-grained sand (Fig. 3d, o) Bed thickness: cm to dm	Ripple cross lamination with sometimes oscillatory ripples at top Lenticular bed Erosive base	Tractive current, current ripples sometimes reworked by oscillatory current influences
Fine			
F	Clay to silt Bed thickness: cm to dm	Massive or thinly laminated clay Planar or inclined bed	Deposition from suspension
Fl	Silty clay to very fine-grained sand with mm to cm beds of fine to medium-grained sand exceptionally coarse-grained and sometimes thin bed of carbonate (Fig 3b, 3d) Bed thickness: cm to dm	Thinly laminated Sandstone beds are massive or contain ripple cross lamination Carbonate bed are massive Sometimes disturbed/homogenised, convolute/contorted bedding, faulted or chaotic and shearing features	Deposition from suspension alternating with tractive current, low density turbidity current (Lowe, 1982)
Fc	Silty clay to very fine-grained sand with mm to cm coal and plant fragments, mm to cm beds of fine to medium-grained sand and sometimes thin bed of carbonate (Fig. 3b, 3o) Bed thickness: dm to m	Thinly laminated Sandstone beds are massive Sometimes disturbed/homogenised, convolute/contorted bedding, faulted, or chaotic features	Deposition from suspension alternating with tractive current, low density turbidity current (Lowe, 1982)
Fr	Sand to clay, reddish to greenish, often rich in mica flakes (Fig. 3p) Bed thickness: cm to m	Massive, disturbed Sometimes with gley structures	Deposition from suspension and pedogenesis
Other facies			
C	Coal with plant fragments and mm to cm beds of fine to medium-grained sand (Fig. 3e) Bed thickness: dm to m	Massive or thinly laminated	Coal deposits alternating with overbank
T	Ochre clay, sometimes with coal chips (Fig. 3e) Bed thickness: cm to dm	Massive or thinly laminated	Volcanic ashes sometimes reworked
Cs	Carbonate	Undulatory bedding	Stromatolite
Cd	Carbonate	Following or cutting through the sedimentary layering	Diagenetic

Tab. 2 Facies description and interpretation of the depositional processes.

21

Code	Facies association	Depositional environment
FP	C, F, Fl, Fc, T, thin layers of Sl, Cd (Fig. 3e)	Swamp
AF	Gmm1, Smm, F, Fl, Fc, C, T, rare GFd (Fig. 3c)	Alluvial fan within swamp or lake (Blair and McPherson, 1994; Miall, 1996)
PL1	Smm, Gmm2, F, Fl, Fr, rare GSm	Unconfined stream flood: distal alluvial fan within a playa lake
PL2	Smm, F, Fl, Fr	Unconfined stream flood: distal alluvial fan within a playa lake
Dfr	GSm, GSt, GSh, Sl, F, Fl, Fc, C, T, rare Smm, GFd (Fig. 3a)	Unconfined flow of delta-front with coal preservation (Postma, 1990; Bhattacharya, 2010)
Dfo	IGSm, IGSt, F, Fl, Fc, rare Smm, GFd, C (Fig. 3b)	Foreset of delta (Postma and Roep, 1985; Rubi et al., 2018)
Dbo	GFd, GSm, GSh, Smm, Sl, F, Fl, Fc, rare C, Gmm2	Bottom set of delta (Postma and Roep, 1985; Rubi et al., 2018)
L1	F, Fl, Fc, thin layers of Sl, GSh, GSm, (Fig. 3d), GFd	Lake with sediment supply deposited laterally to the delta
L2	F, Fl, Cs, C, GFd	Lake environment with rare stromatolites or carbonate layers or more frequently few sediment supply with soft-sediment deformation

Tab. 3 Facies associations identified within the LY-F core and their attribution to depositional environments.

4.1. ***Facies associations and depositional environments***

From the base to a depth of 581 m (Fig. 2), the core is mainly composed of sandstones and conglomerates interbedded with thin siltstone and coal layers. The coarser facies are either massive (GSm and IGSm facies, Table 2; Fig. 3a, b) or constituted by 3D megaripples (GSt and IGSt facies, Table 2; Fig. 3a) or locally by horizontal laminations (GSh facies, Table 2). The GSt, GSh and GSm facies are stacked together (Fig. 3a) or interbedded with thin fine facies levels (Fl, Fc facies), and sometimes with thin coal layers (C facies). The inclined facies (IGSt and IGSm; Fig. 3b) are isolated within inclined Fl facies and display soft-sediment deformations (SSD), such as convolutes, balls and pillows and both slumps, and shearing-related structures that can correspond to chaotic beds (GFd, Table 2). From 589 to 590 m, occurrence of the fine (Fc) and coal (C) facies are more common, and the coarse facies are completely absent. As a consequence, three facies associations can be recognised within this first part of the section. The first facies association, named Dfr (Fig. 3, Table 3), is mainly characterised by tractive processes (GSt, GSh) with some debris flows (GSm, Smm, Fig. 3a, f, i) typical of unconfined flows in delta-front deposits (Postma, 1990; Bhattacharya, 2010), associated with swamp recorded by coal preservation. The second facies association, named Dfo (Fig. 2, Table 3), is composed of inclined beds representing foreset deposits and recording periods of gravity processes (IGSm, Fig. 3b) alternating with settling of particles (Fc or Fl, Fig. 3b), with some hydraulic jump (IGSt) and slump occurrences, typical of delta deposits (Postma and Roep, 1985; Rubi et al., 2018). The facies association marked by the development of siltstone and coal layers (F and C facies, Table 2) is named FP (Fig. 2, Fig. 3e, Table 3), and is attributed to a humid floodplain with swamp deposits.
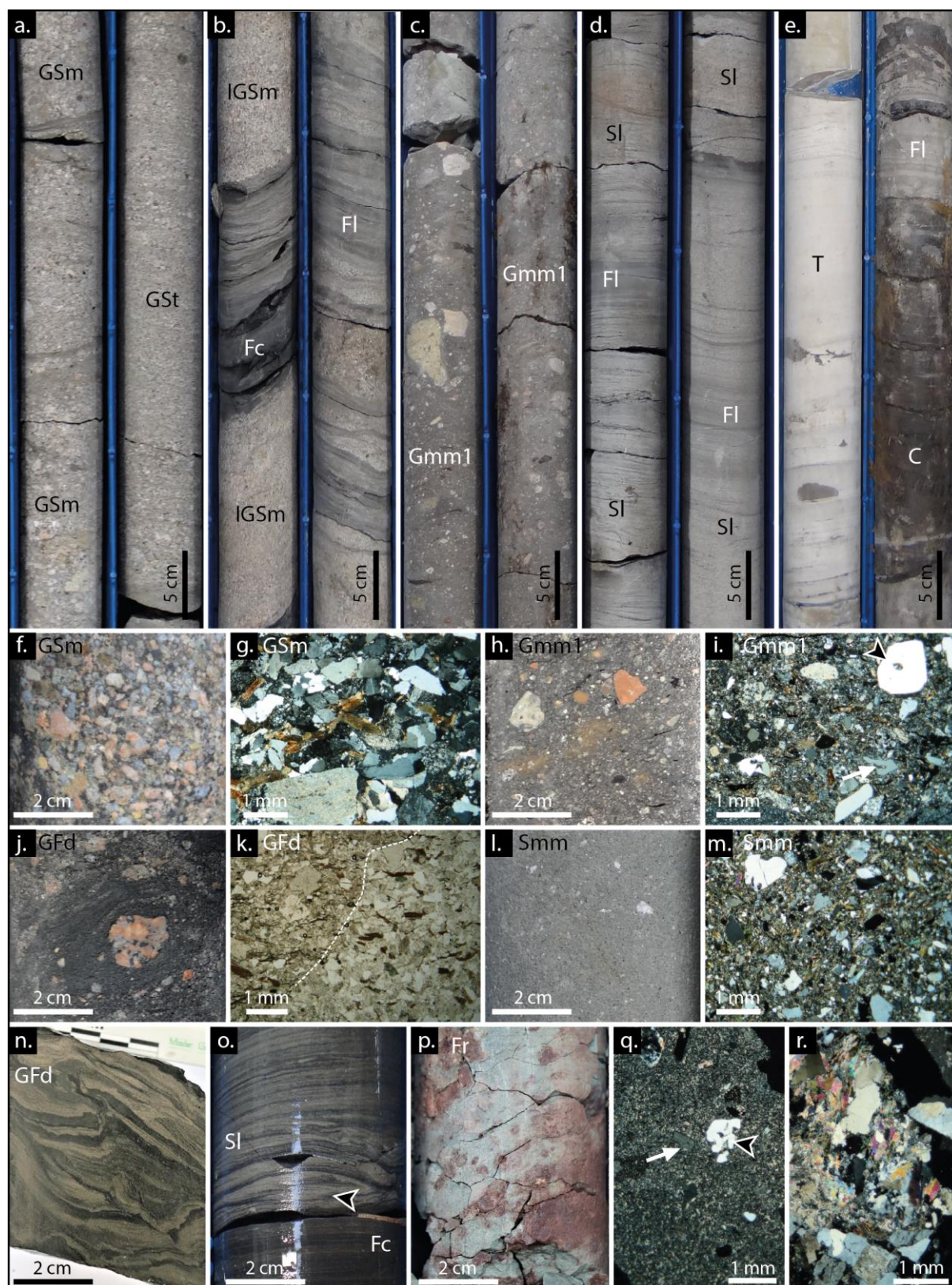
Fig. 3 Overview photographs of the facies identified within the LY-F core (the top is

above): a) GSm and GSt facies; b) IGSm, Fc and Fl facies; c) Gmm1 facies; d) Fl and Sl facies;

e) T facies; f) Fl and C facies; Details of f & g) GSm facies (f: macrosample; g: thin section,

cross-polarized light (hereafter XPL), note the angular shape and the relatively good sorting of the grains compared with the Gmm1 and Smm facies); h & i) Gmm1 facies (h: macrosample; i: thin section, XPL, note the occurrence of volcanic quartz grains with a subhedral shape (black arrow) and/or corroded surfaces (white arrow)); j & k) GFd facies within coarse-grained sandstones displaying post-depositional mixing of layers with different grain-sizes (h: macrosample, note the large clast surrounded by laminated finer-grained sediments; i: thin section, plane-polarized light (hereafter PPL), oblique contact underlined by a dashed white line); l & m) Smm facies (l: macrosample; m: thin section, XPL, note the occurrence of angular quartz and small flakes of white micas); n) GFd facies within fine deposits: thin layers affected by both brittle and ductile deformation related to slumping; o) Finely laminated Fc and Sl facies with small ripples; p) Fr facies with gley structures; q) Cryptocrystalline volcanic rock fragment with quartz (black arrow) and feldspar (white arrow) phenocryts (thin section, XPL); r) Muscovite-rich rock fragment with quartz and feldspars (thin section, XPL).

From 581 m to ~ 560 m (Fig. 2), the coal and fine-grained facies dominate and are interbedded with layers of volcanic ashes (T facies, Table 2; Fig. 3e). At the base, a new facies association appears, characterised by the occurrence of the Gmm1 facies (Fig. 3c, h), typical of cohesive debris flows, with load-cast and shear-related structures, and interbedded with thin fine (F facies) and coal (C facies) layers. This facies association, named AF (Fig. 2, Table 3), corresponds to alluvial-fan delta deposits within lake or swamp (Nemec, 1990). This environment evolves to coal with fine facies intercalations, typical of swamp deposits of the FP facies association (Fig. 2, Table 3).

From 560 to 533 m (Fig. 2), two new facies associations appear. The first one is composed of fine facies (Fl, Fc facies) with occurrence of stromatolite layers (Cs facies,

Table 2). Occurrences of diagenetic carbonates (Cd facies, Table 2) are also observed within the fine facies. The second facies association is also composed of the same fine facies alternating with thin sandstone facies layers (mainly Sl facies, Fig. 3d, o, with few GSm, GSh or GFd facies, Fig. 3d, o). The predominance of fine facies, with coal and plant reworking, stromatolites, and some occurrences of sandstones with current ripples, locally reworked by oscillatory currents, implies a depositional environment within a water level. Both facies associations represent a lake environment, either with some sediment supply and deposited laterally of the delta (L1 facies association; Fig. 2, Table 3), or with a weak sediment supply, deposited far away from the delta-front (L2 facies; Fig. 2, Table 3).

From 533 to 494 m (Fig. 2), the depositional environment, mainly marked by thick conglomeratic deposits (Gmm1 facies; Fig. 3c, h) associated with minor fine facies and thin volcanic ash and coal layers (Fl, Fc, T, C facies, Table2), corresponds to alluvial-fan delta within a swamp or a lake environment (AF facies association, Table 3). From 494 to 485 m (Fig. 2), the depositional environment changes progressively, as recorded by thinner conglomerate and sandstone (Gmm1, Smm facies) layers interbedded within thicker fine and coal layers and volcanic ashes, corresponding to a transition between the AF (alluvial-fan delta) and FP (flood plain) facies association.

From 485 to 446 m, the swamp environment (FP facies association, Table 3) with thick coal layers and volcanic ashes (C, T facies, Table 2) are alternating with fine-grained sediments with less coal layers (F, Fl, and Fc facies, Table 2). The absence of medium- to coarse-grained facies implies to assign these deposits to the L2 facies association (Fig. 2, Table 3) corresponding to a more distal lake environment (i.e., with less sediment supply than L1). Indeed, the occurrence of stromatolites (Cs facies) associated with disturbed

layers and contorted beds (Fig 3n) suggests that deposition took place under low water level.

From 446 to 400 m (Fig. 2), a new facies association appears, characterised by the predominance of gravel to fine facies affected by SSD (GFd facies, Table 2; Fig 3j, n), interbedded with gravity deposits (GSm, Gmm2 or Smm facies) and fines (Fl, Fc facies) with numerous load-cast, ball and pillow and dewatering features. One tonstein layer is observed at around 413 m. This facies association, named Dbo (Fig. 2, Table 3), is interbedded with foreset delta (Dfo) and delta-front (Dfr) facies associations, and is therefore attributed to the bottomset deposits of the delta system (Postma and Roep, 1985; Rubi et al., 2018). In consequence, this core interval records an evolution from delta deposits with foreset and bottomset deposits (Dfo and Dbo, Fig. 2) to delta-front related deposits with episodic coal preservation (Dfr, Fig. 2).

From 400 to 316 m, several trends are observed with an evolution from lake facies (L2 facies association) to delta facies (Dbo, Dfo, Dfr facies associations, Table 3), and locally to swamp deposits (FP facies association, Fig. 2). Here, the lake facies (L2 facies association) are usually followed by delta bottomset deposits (Dbo facies association) and are not associated with stromatolites, suggesting that they may correspond to a distal and deep lacustrine environment.

From 316 m to the top of the core, the fine facies are locally reddish, while coal and volcanic ash layers are absent. The occurrence of high-density turbidite deposits (Gmm2, Smm facies, Table 2) interbedded with fine facies (F and Fl facies, Table 2) corresponds to unconfined stream floods that represent sandsheet deposits within a lake. However, the reddish fine facies (Fr; Fig. 3p) locally preserve gley structures suggesting hydromorphic soil development. The facies association (Fl, F, Fr, Smm, Gmm2, GSm) therefore attests lake level fluctuations with periods of emersion and corresponds to

27

sediment supply within a playa-lake environment. Two facies associations are distinguished, named PL1 and PL2 for proximal and distal playa-lake environments, respectively (Table 3). At the top of the core section, some delta front and delta foreset facies associations are also present (Dfr and DFo facies associations, Table 3).

4.2. Petrographic study

A semi-quantitative petrographic analysis was performed on 29 sandstone and conglomerate samples collected from the LY-F core (see location of the samples on Fig. 2). Results are provided in Table 4 and Figure 4. Sandstones and conglomerates from the GSm facies are relatively well-sorted, clast-supported and consist of feldspathic or lithic arenites (Fig. 3g; Fig. 4a, QFM diagram, classification from Dott, 1964). The main components are quartz (28 to 48 %), sericitised plagioclase and untwinned and/or perthitic alkali feldspar (20 to 33 %) and lithic fragments (13 to 32 %), mainly of volcanic origin, although towards the top of the core muscovite-rich rock fragments predominate (Fig. 3r). Phyllosilicates are also common (5 to 18 %) and mainly consist of biotite and chlorite, while muscovite content increases significantly towards the top of the core.

Sandstones and conglomerates from the Gmm1 (Fig. 3i), Gmm2 and Smm (Fig. 3m) facies are poorly-sorted and matrix-supported, and mainly consist of lithic wackes, although samples taken in the top 50 m of the core correspond to feldspathic wackes (Fig. 4b, QFM diagram, classification from Dott, 1964). The matrix, made of particles smaller than 1 mm for the Gmm1 and Gmm2 facies and smaller than 500 μm for the Smm facies, ranges between 25 and 65 %. In samples located in the lower part of the core (Gmm1 facies and 1 sample from the Smm facies), elements mainly consist of rock fragments (up to 35 %), mainly of volcanic origin (Fig. 3q), quartz (up to 20 %) and minor feldspars (up to 5 %). In samples from the top of the core (Smm and Gmm2 facies),

elements mainly consist of quartz (up to 83 %) and minor feldspars (up to 28 %), rock fragments (up to 17 %), with many mica-rich fragments (Fig. 3r) and micas (mostly white micas, Fig. 3m).

Sample	Facies	Matrix (%)	Quartz				Feldspars			Micas					Rock Fragments					Coal Fr (%)
			Volc (%)	Ang. (%)	Pol. (%)	TOT Qtz	Plag (%)	Alk (%)	TOT Fdp	Bi (%)	Bi+cal (%)	Mu (%)	Ch (%)	TOT Mica	Volc 1 (%)	Volc 2 (%)	Plu/Met (%)	oth*	TOT RF	
LYF 593	GSt/IGSt	-	3	20	15	38	12	14	26	10	1	1	1	13	6	15	2	-	23	-
LYF 592	GSm/GSh	-	3	20	16	39	18	15	33	5	8	-	2	15	3	8	2	-	13	-
LYF 577	Gmm1	60	6	2	-	8	2	2	4	-	-	-	-	-	10	10	5	-	25	3
LYF 532	Gmm1	40	11	5	2	18	3	2	5	-	-	-	-	-	10	24	-	-	34	3
LYF 519	Gmm1	65	4	2	1	7	2	1	3	-	-	-	-	-	5	15	2	-	22	3
LYF 515	Gmm1	45	12	5	1	18	2	3	5	-	2	-	-	2	10	15	2	1	28	2
LYF 511	Gmm1	55	4	1	-	5	2	-	2	-	-	-	-	-	10	18	6	-	34	4
LYF 501	Smm	60	12	5	-	17	3	2	5	-	-	-	-	-	8	10	-	-	18	-
LYF 497	Gmm1	55	3	2	1	6	2	1	3	2	-	-	-	2	13	11	6	-	30	4
LYF 446	GSm d	15	4	12	12	28	8	20	28	10	-	-	-	10	10	8	1	-	19	-
LYF 437	GFd	-	2	15	16	33	6	22	28	7	-	1	2	10	16	6	6	1	29	-
LYF 428	GSm	10	-	-	-	-	-	-	-	-	-	-	-	-	35	30	25	-	90	-
LYF 419	GSm	-	1	15	20	36	12	15	27	12	-	-	3	15	10	5	2	-	17	5
LYF 406	GFd	-	2	18	16	36	5	22	27	10	-	-	5	15	10	10	2	-	22	-
LYF 403	GSm	-	1	20	10	31	10	15	25	12	-	-	6	18	10	15	1	-	26	-
LYF 381	GSm	-	3	12	18	43	6	26	32	5	-	-	-	10	15	10	-	-	20	-
LYF 374	GFd	-	3	15	12	30	5	22	27	5	4	-	2	11	18	14	-	-	32	-
LYF 370	GFd	-	2	12	15	29	5	20	25	6	-	-	3	9	16	11	6	-	33	4
LYF 344	GSm	-	5	12	15	32	2	20	22	6	-	-	3	9	18	14	5	-	37	-
LYF 340	Sl	-	-	18	-	18	12	18	30	10	1	4	2	17	13	22	-	-	35	-
LYF 313	GFd	25	2	15	10	27	-	10	10	6	-	3	4	13	8	10	2	5	25	-
LYF 306	GSm	-	2	15	12	29	11	10	21	8	-	-	4	12	26	10	-	-	36	2
LYF 296	Smm	75	-	12	6	18	-	2	2	-	-	2	1	3	-	-	-	2	2	-
LYF 292	GSm	-	2	25	20	47	10	10	20	6	-	5	5	16	-	-	2	15	17	-
LYF 292	Smm	70	-	14	6	20	-	5	5	-	-	2	-	2	-	-	-	3	3	-
LYF 280	Smm	85	-	10	-	10	-	-	-	2	-	1	-	3	-	-	-	2	2	-
LYF 274	GSm	-	3	20	25	48	2	20	22	2	-	4	-	6	4	10	10	-	24	-
LYF 267	GSm	-	0	22	27	49	18	15	33	1	-	0	0	1	5	2	0	10	17	-
LYF 265	Gmm2	25	6	22	12	40	8	12	20	-	-	3	-	3	8	2	2	-	12	-

Tab. 4 Semi-quantitative analysis of the sandstones and conglomerates from the LY-F core.

Samples from the Gmm1 facies contain significantly more quartz with features suggesting a volcanic origin (i.e., euhedral grains with slightly rounded edges and corrosion gulfs; Fig. 3i) than samples from the GSm, GFd and Gmm2 facies, in which angular and polycrystalline quartz grains are more common (Fig. 4c). Samples from the GFd facies have a similar composition than those from the GSm facies; they consist of an

alternation of layers (from fines to conglomerates) affected by SSD, and therefore displaying either irregular contacts between the different lithologies (Fig. 3k), or injections of fine-sediments between coarser grains, and conversely. When mixing is intense, the GFd facies may display a poorly-sorted texture and therefore be mistaken with the Gmm1 or Gmm2 facies.

To sum up, the Gmm and Smm facies are mainly characterised by a poor sorting when compared to the GSm and Sl facies. The mineral compositions of these different facies change significantly with depth, with an increase in quartz and muscovite contents towards the top of the core, recorded in both GSm and Gmm/Smm facies. Rock fragments of volcanic origin are found in most samples, but are predominant in samples from the Gmm1 facies, which also contain a large amount of quartz of volcanic origin.
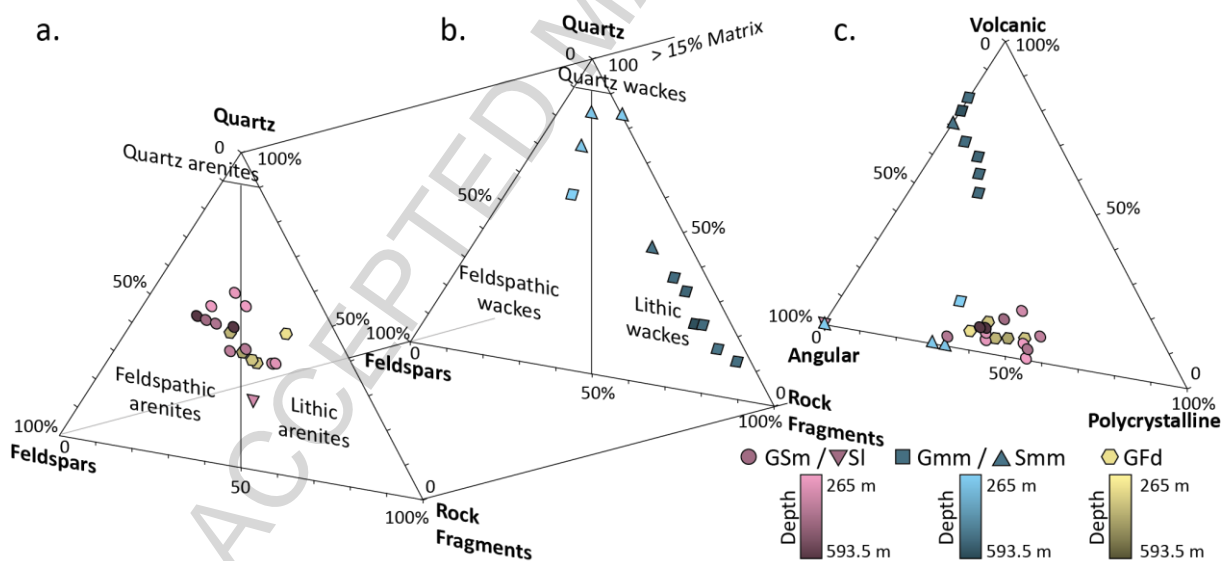
Fig. 4 a) QFM diagram for sandstones and conglomerates with less than 15 % of matrix, and b) with more than 15% of matrix (classification of terrigenous rocks from Dott, 1964); c) Ternary diagram showing the relative proportion of volcanic, angular and polycrystalline quartz grains in sandstones and conglomerates

4.3. Depositional environments evolution

The facies associations described above and assigned to different depositional environments are used to reconstruct the palaeo-environmental evolution of the area, as illustrated on the detailed sedimentological section (Fig. 2) or on the synthetic section (Fig. 5). The more proximal environment is attributed to a floodplain, mainly characterized by swamp with coal and volcanic ash layers expressed as tonsteins (FP, Table 2). The sediment supply is inherent either to delta processes (DF, Dfr, Dfo or Dbo, Table 2) or to alluvial fan deposits (AF, Table 2). The alluvial fan delta deposits contain much more volcaniclasts (volcanic quartz grains, volcanic rock fragments) than the delta sediments, suggesting that they derive from a different source, mostly volcanic in origin. These alluvial fan sediments are therefore attributed to volcaniclastic mass flows. Their close association with tonstein layers and the fact that these volcaniclastic deposits are only found as debris flows suggest that they correspond to catastrophic events that were deposited during periods of volcanic activity. However, in the absence of geochronological constraints for the volcaniclasts, it cannot be excluded that at least part of the volcaniclasts could have been reworked from older volcanic deposits (e.g., Rossignol et al., 2019). Lake deposits (L1 and L2) or playa-lake (PL1 and PL2 facies associations) are either located laterally from the delta, where detrital input is weaker, or in the more distal part of the lake. The distinction between L1/PL1 and L2/PL2 facies associations is only based on the detrital input and not on the water depth of the lake, nor on the distance from the coastline. When stromatolites are clearly identified, a proximal position and a low water depth is inferred. However, some of the thin carbonate layers often found in the lake deposits have a diagenetic origin and should not be mistaken for stromatolites. Some volcanic ash layers (tonsteins) are also observed in the lake environment.
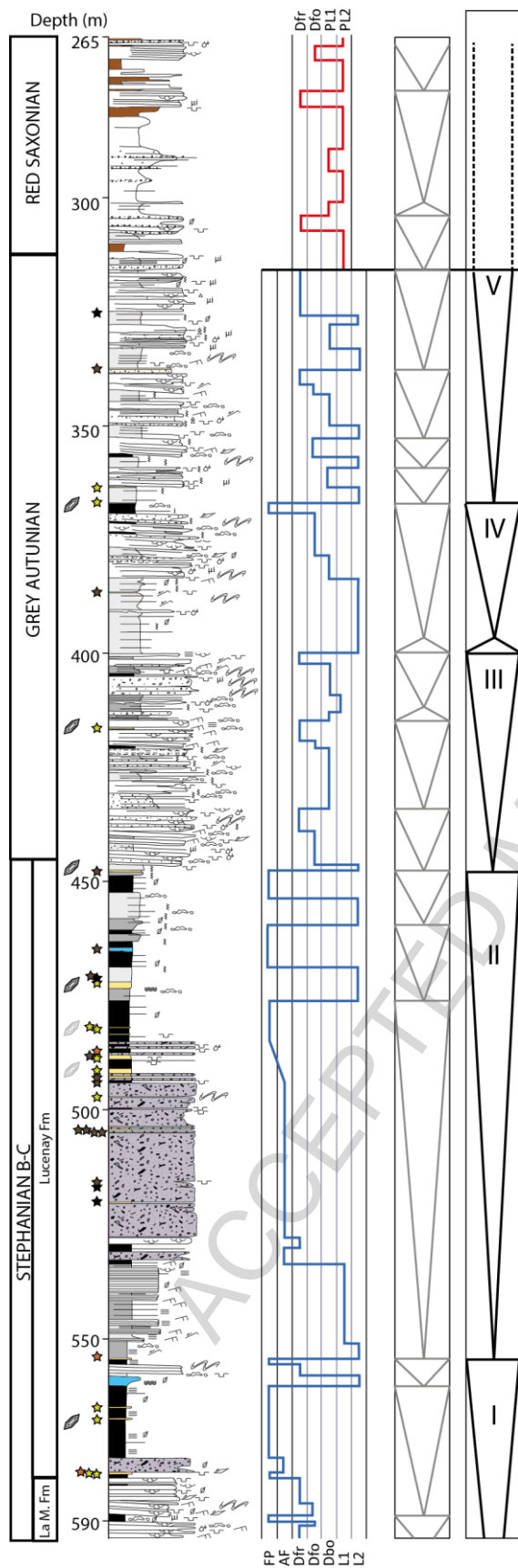
31

Fig. 5 Synthetic log of the LY-F core with the depositional profile and stratigraphic cycles. The attribution to the different units and formations is from Donsimoni (1990); see legend on Fig. 2.

Two depositional profiles have been drawn: one from the base to 316 m, characterised by floodplain (FP) to delta (DF, Dfr, Dfo, Dfbo) and lake deposits (L1, L2); and the second from 316 m to the top, from delta (Dfr, Dfo) to playa-lake deposits (PL1, PL2).

The evolution of the depositional profiles (Figs. 2 and 5) from the base to the top of the core, displays five major progradational/retrogradational cycles (noted I to V, Fig. 5), for which progradational trends are particularly well preserved.

From 593.5 to 560 m, the first cycle, noted I (Fig. 5), records only a progradational trend with a well-developed coal level at its upper part. It is composed of three minor progradational trends, with delta facies associations (delta-front, Dfr, and foreset, Dfo, deposits, Table 2) and swamp deposits characterising the floodplain facies association (FP, Table 2). It ends with a small progradational trend from shallow lake with stromatolites layers (L2, Table 2) to front-delta delta (DFr, Table 2) and then floodplain (FP) facies association.

From 560 to around 449 m, the second cycle trend, noted II (Fig. 5), is composed of three minor cycles where only progradational trends are recorded. The first one is well-developed and mainly consists of thick lake deposits (L1), followed by thick volcaniclast-rich alluvial-fan deposits (Gmm1 facies of the AF facies association, Table 2), and evolving progressively to swamp deposits with several volcanic ash layers (FP facies association, Table 2). The last two minor cycles are short and consist of a progradational trend from lake deposits with a weak sediment supply of the L2 facies association to swamp deposits (FP facies association). These two cycles do not represent necessarily a high relative lake

33

level variation, as the lake environment may correspond to littoral deposits, as suggested by the occurrence of stromatolites.

The third cycle, from 449 to ~400 m, noted III (Fig. 5), is also marked by a well-developed progradational trend from lake (L2 facies association, Table 2) to delta facies associations (from delta-front, Dfr, foreset, Dfo, and bottom set, Dbo, deposits, Table 2); a short retrogradational trend is recorded within lake deposits, at the top of this cycle. Cycle III is divided into three minor cycles, where the progradational trends are well-developed and the retrogradational trends are either short or not recorded. Within these cycles, coal layers are thin and ash layers are rare.

The fourth cycle, noted IV, from ~400 to 367 m, is marked by 17 m of well-developed distal lacustrine facies with few sediment supply (L2, Table 2), which evolve progressively to delta facies associations (with bottomset, Dbo and foreset, Dfo deposits, Table 2) and to swamp deposits with coal and ash layers (FP, Table 2).

The fifth and last major cycle, noted V (Fig. 5) starts at 367 m and is possibly recorded up to the top of the core. The lower part records a progradational trend, up to 314 m. It can be divided in four minor cycles for which only progradational trends, from lake deposits (L2 facies association, Table 2) to delta deposits (Dfr, Dfo and Dbo facies associations, Table 2) are recorded. Then, from 314 m, the depositional profile changes: three minor cycles displaying mainly progradational trends, from dominant playa-lake deposits (PL2 and PL1 facies associations, Table 2) to poorly developed delta deposits (Dfr and Dfo facies associations, Table 2), are recorded. This change is also marked by a compositional change of the detrital minerals, characterised by an increase of quartz and muscovite contents and a change in the nature of the lithic fragments. However, as these observations are close to the top of the core, it is difficult to know if these cycles belong to the same progradational trend or if they already belong to a retrogradational trend.

5. Geochronological constraints

5.1. Identification of tonsteins from mineralogical and geochemical analyses

Among the 33 clay layers analysed by XRD (bulk and clay-size fractions, Table 1), 13 correspond to pure tonsteins (e.g., mainly composed of kaolinite, with little up to 40% of IS R1, and minor quartz and feldspar, Table1, Fig. 6a). In addition, 16 clay layers are considered as mixed tonsteins, consisting of a mixture of volcanic ashes incorporating variable proportions of detrital particles. Out of these 16, 3 layers present only traces (<1–2%) of illite in the clay fraction, which is considered as detrital and reworked from soil or old basement rocks (LYF579.35, LYF554.34 and LYF487.25, Table 1), suggesting a weak detrital contamination, while 13 are composed of a mixture of authigenic volcanogenic clay minerals and detrital minerals marked by more than 2 % of illite in the clay fraction and/or of mica-illite in the bulk fraction (Table 1, Fig. 6b). The last 4 analysed clay layers do not present clear evidence for a volcanogenic input as they are characterized by a common detrital mineralogy (illite, R1 IS, CV, kaolinite, chlorite and more abundant quartz in the bulk fraction, Table 1, Fig. 6c).

The 13 pure tonsteins from the LY-F core display the same mineralogical features than those observed in the Carboniferous–Permian series of the Autun Basin (Pellenard et al., 2017) (Fig. 1b). Geochemical analyses (Supplementary material 1) were performed on 10 pure tonsteins and on 1 mixed tonstein layer containing traces of illite (LYF554.34). Most tonstein samples present similar geochemical signatures than the samples from the Autun Basin (Fig. 7a, b, c), although four of them (LYF367.15, LYF481.95, LYF482.15, LYF579.6) display differences marked by (i) a slightly higher Nb/Y ratio (Fig. 7a), (ii) a slightly higher Ta concentration relative to Hf and Th (Fig. 7b) and (iii) a lower Yb

concentration (Fig. 7c). In addition, the low TiO_2/Al_2O_3 ratio of these tonsteins (<0.02)

suggest that the original ashes were silica-rich. These trends are similar to those recorded

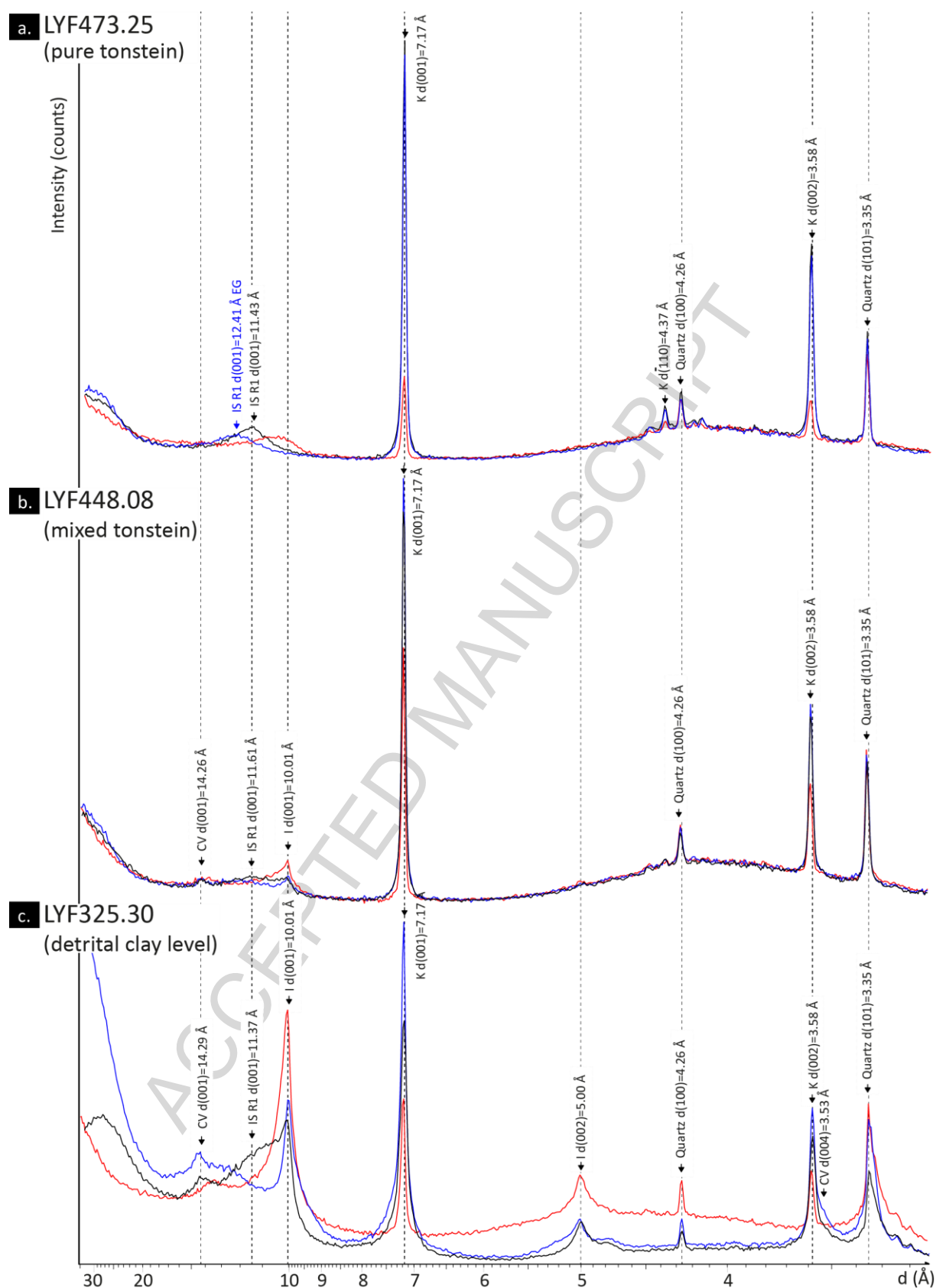from tonsteins mixed with detrital input sampled in the Autun Basin (Fig. 7a, b, c).

Fig. 6 Comparison of XRD diffractograms showing examples of (a) a pure tonstein (LYF473.25), (b) a mixed tonstein with detrital particles (LYF448.08) and (c) a detrital

clay level (LYF325.30). Black, blue and red lines are for air dry, glycolated solvation and heated (490°C) conditions, respectively. CV = chlorite-vermiculite mixed-layer; R1 IS = R1 type illite-smectite mixed-layer; I = illite; K = kaolinite.
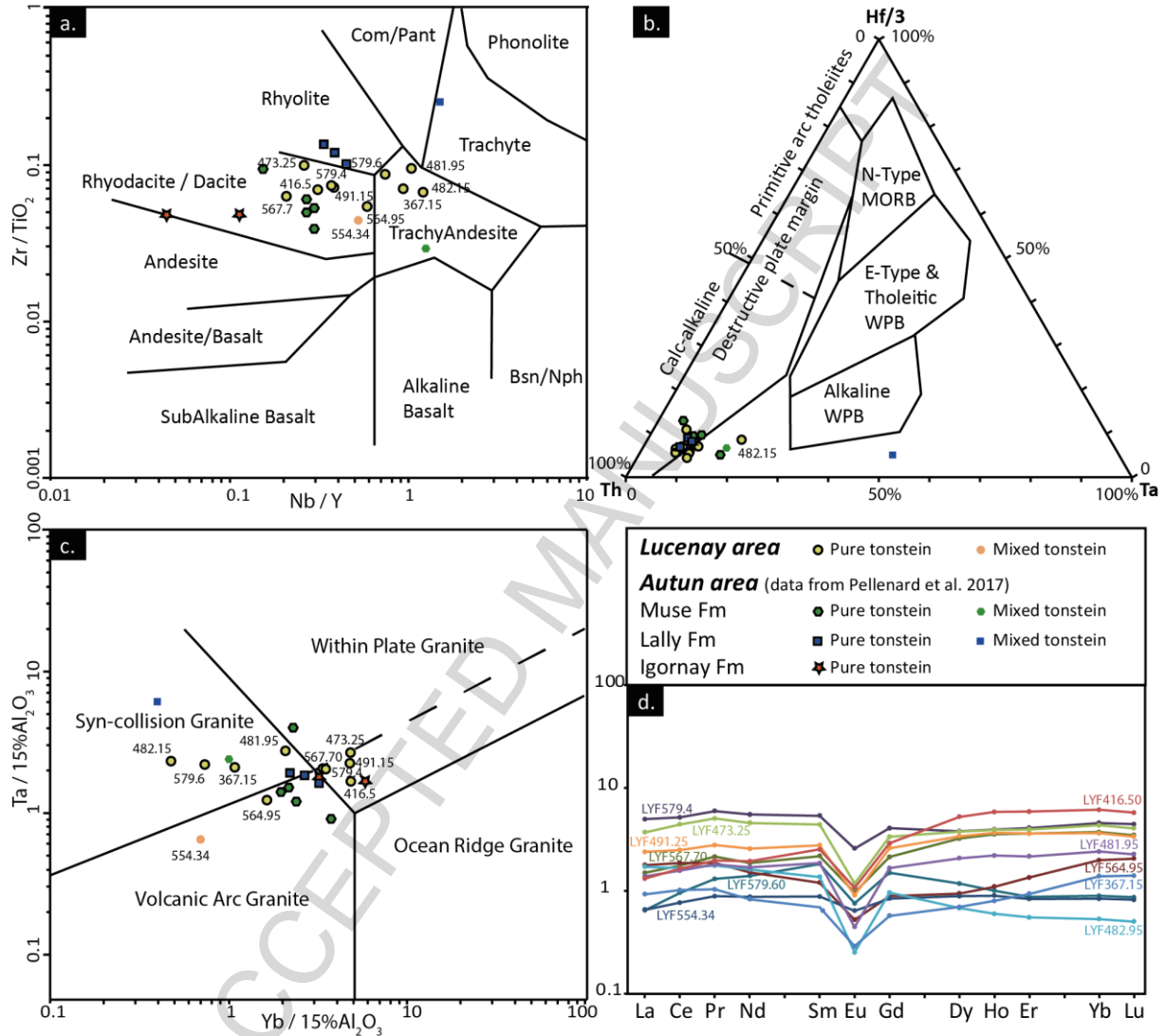
Fig. 7 Geochemical data from 11 tonsteins from the LY-F core (Lucenay-lès-Aix area) compared with the data from Pellenard et al. (2017) for the Muse, Lally and Igornay sections in the Autun Basin a) Zr/TiO$_2$ vs Nd/Y diagram (Winchester and Floyd, 1977) indicating the chemical nature of the magma; b) Th-Ta-Hf/3 ternary diagram (Wood, 1980) and c) Ta vs Yb (normalised to 15% Al$_2$O$_3$) diagram (Pearce et al., 1984) indicating

the tectonic context; and d) REE profiles normalised to the Cody-shale (Jarvis and Jarvis, 1985)

However, XRD analyses for the LY-F samples did not evidence a contamination by detrital input but present a high content in kaolinite that may suggest a more intense leaching after deposition. Additionally, the tonstein samples from the LY-F core are characterised by negative Eu anomalies in the REE pattern (Fig. 7d), which are also recognised in tonsteins from the Autun Basin (but absent in the enclosing sediments, Pellenard et al., 2017) and in most tonstein deposits (Bohor and Triplehorn 1993). This negative Eu anomaly is less marked for the mixed tonstein LYF554.34, which is consistent with a contamination by detrital input, as revealed by XRD analyses.

Seven tonstein samples have been selected for geochronological analyses. Their location is reported on Figures 2 and 5. The selection criteria of these tonsteins are (i) their stratigraphic position, (ii) the degree of contamination by detrital input visible by XRD and geochemical analyses, and (iii) the amount of material available for mineral separation. According to the XRD analyses, 6 of the selected samples (LYF567.7, LYF491.25, LYF482.15, LYF473.25, LYF416.5 and LYF367.15) correspond to pure tonsteins. The seventh sample (LYF448.08) has been selected for its intermediate stratigraphic position despite the fact that it corresponds to a mixed tonstein, with evidence for a weak contamination by a detrital component (2% of mica/illite in the bulk fraction and 6% of illite in the clay fraction (Table 1).

5.2. U-Pb on zircon and apatite

Out of the seven tonstein samples selected for geochronological analyses, five (LYF567.70, LYF473.25, LYF448.08, LYF416.5 and LYF367.15) contained enough zircon

grains to proceed with LA-ICP-MS analyses. Two samples (LYF491.5 and LYF482.15) were exempt of any zircon grain. Additionally, apatite grains were hand-picked for 3 of these samples (LYF448.08, LYF416.5 and LYF367.15).

The size of the zircon grains is quite variable, with very large grains (200 µm in average, up to 600 µm) for sample LYF567.15, large grains (75 µm in average, up to 250 µm) for sample LYF473.25, LYF448.08 and LYF416.5 and small grains (50 µm in average, up to 100 µm) for sample LYF367.15. Most of the grains are euhedral, often elongated, with length-to-width ratios ranging from 2 to 8, suggesting a rapid crystallization for the most elongated (Corfu et al., 2003). Cathodoluminescence (CL) imaging reveals that most of these crystals have a broad-band blue CL emission and present a growth zoning, although some present only a faint zoning. A few zircon grains present zoning discontinuities, suggesting occurrences of small, often dark, xenocrystic cores. However, such features may also be generated by several episodes of resorption and growth of the zircon crystal in the magmatic chamber, due to changes in the saturation of the magma with respect to Zr (e.g., Corfu et al., 2003).

Apatite grains range in size from a few tens to a few hundreds of micrometres. They are usually euhedral, prismatic and often elongated. Almost all apatite grains exhibit a homogeneous blue/violet CL colour and zoning is not revealed by CL imaging.

Results of U-Pb dating on zircon and apatite are shown on Figures 8 and 9 respectively and are described below from bottom to top. Data from zircon and apatite analyses are provided in Supplementary material 5 and 6, respectively.

In sample LYF567.70, 20 out of 40 analysed zircon grains are concordant (Fig. 8a, b). These data, when plotted in a Tera-Wasserburg diagram, form a well-defined cluster yielding a concordia date of 299 ± 2 Ma (n = 17, MSDW = 0.35; Fig. 8b). Three zircon

analyses were discarded. Two slightly younger concordant zircon analyses (at 277 ± 6 and 285 ± 7 Ma) are interpreted as resulting from Pb loss. One grain also yielded a slightly older date (313 ± 8 Ma) and could correspond either to a xenocryst incorporated into the magma by assimilation of its surrounding host rocks, an antecryst that crystallized during an earlier evolution stage of the same magmatic system (e.g., Miller et al. 2007). An epicrysts grain sourced by the background sedimentary flux is considered unlikely, because XRD analyses reveals that this layer is almost exclusively made up of volcanogenic material. This concordia date is similar to the TuffZirc date (299 +2/−1 Ma; Fig. 8c) although only the 2 younger dates are considered as outliers and are discarded by the TuffZirc algorithm.

In sample LYF473.25, only 8 grains out of 48 zircon grains yielded concordant dates. The other zircon analyses seem to have incorporated common Pb and to a lesser extent, to have been affected by Pb loss (Fig. 8d). Six zircon analyses were used to calculate a concordia date at 298 ±3 Ma (MSWD = 0.16; Fig. 8e), equivalent within error to the TuffZirc date of 298 ±3 Ma using the same zircon analyses (Fig. 8f). The younger and older dates have been discarded as they are considered to result from Pb loss and from inheritance, respectively. Considering that the XRD analyses performed on this sample suggest that it was not contaminated by detrital input, the older zircon grain is considered either as a xenocryst, or more probably as an antecryst, and not as an epicryst.
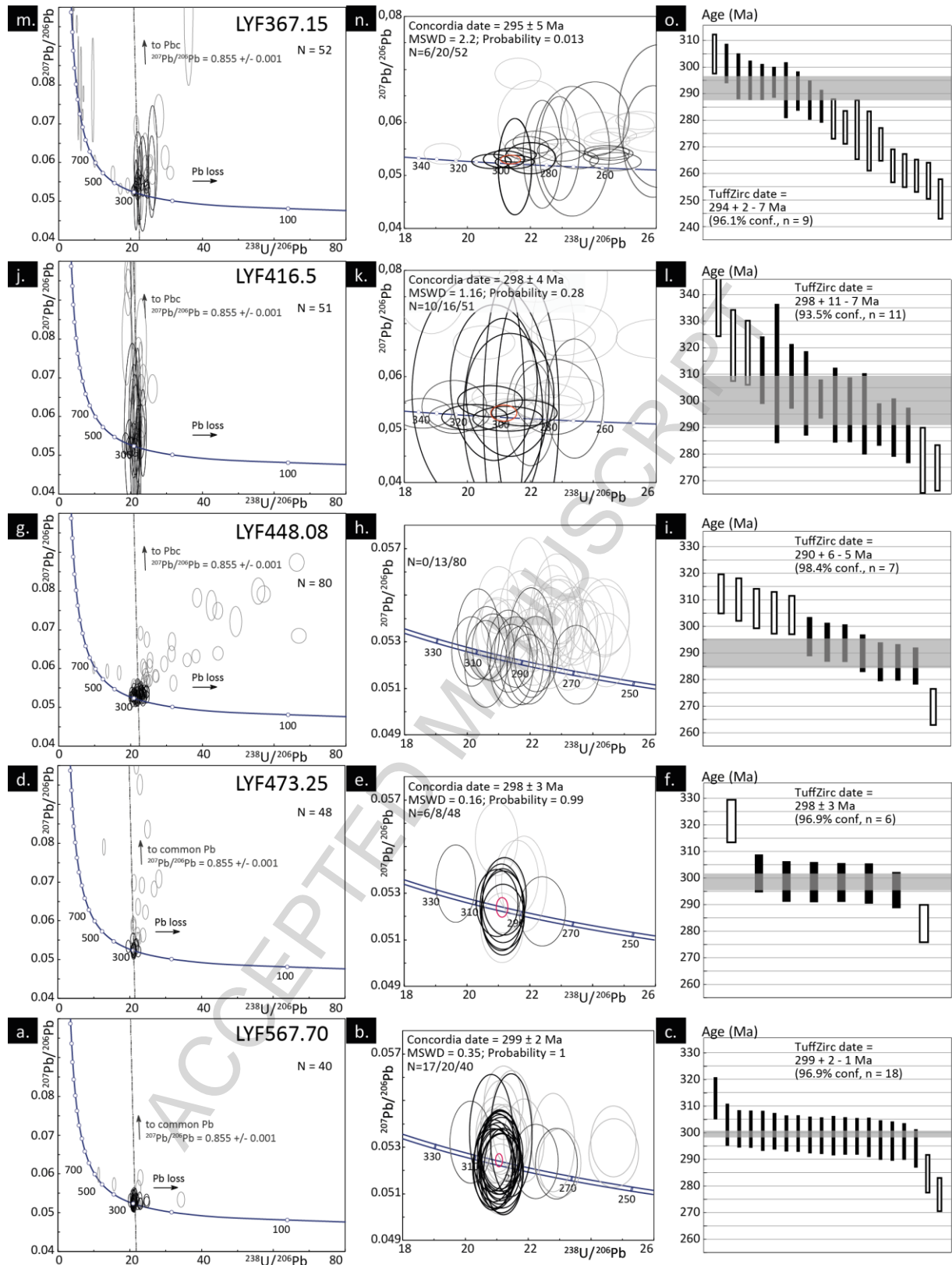
Fig. 8 U-Pb on zircon data for sample a to c) LYF567.70; d to f) LYF473.25; g to i) LYF448.08; j to l) LYF416.5 and m to o) LYF367.15. To the left, all data are plotted on Tera-Wasseburg diagrams displaying concordant zircon analyses (in black) but also zircon

42

analyses that yielded older dates, that incorporated common Pb and/or have been affected by Pb loss (all in grey). In the centre, Tera Wasserburg diagrams are centred on the main cluster of zircon analyses, from which are calculated weighted mean concordia dates, depicted in red (MSWD and Probability are given for both concordance and equivalence; N= number of zircon analysed to calculate the weighted mean concordia date, black thick ellipses / number of concordant data, black ellipses / total number of zircon analyses, grey ellipses). To the right, results provided by the TuffZirc algorithm applied on concordant zircon analyses: the data selected and rejected to calculate the TuffZirc dates are shown in black and white respectively; the grey area correspond to the TuffZirc date and its calculated error. Data point ellipses and error bars are 2 σ.
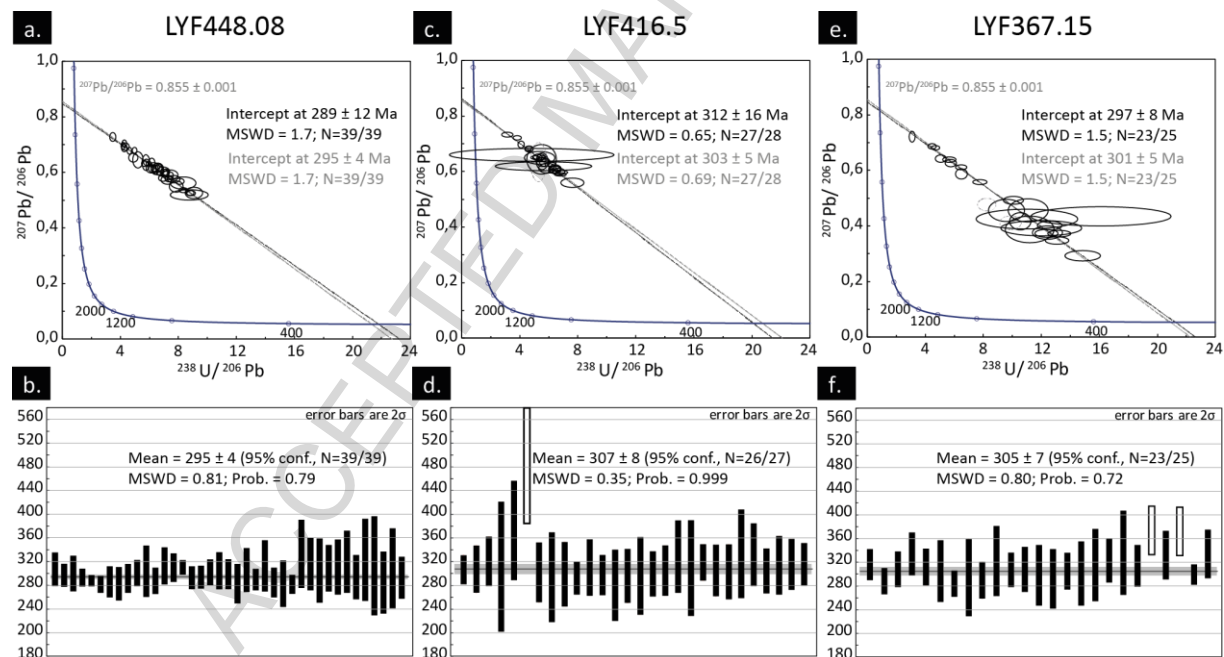
Fig. 9 U-Pb on apatite data for sample a & b) LYF448.08; c & d) LYF416.5 and e & f) LYF367.15. To the top, all apatite analyses are plotted on Tera-Wasserburg diagrams and intercept dates are calculated for both unforced discordia (in black) and discordia for which the upper intercept was anchored to an initial $^{207}Pb/^{206}Pb$ value of 0.855 ± 0.001 (in grey). Apatite analyses rejected for the calculation of the intercept dates are displayed

in dashed grey. To the bottom, weighted-averages dates performed on [207]Pb-corrected dates with a fixed initial [207]Pb/[206]Pb value of 0.855. Rejected analyses are shown in white. Data point ellipses and error bars are 2 σ.

In sample LYF448.08, 80 zircon grains were analysed but only 14 yielded concordant dates (Fig. 8g, h). Discordant zircon analyses seem to have been affected by both Pb loss and the presence of common lead (Fig. 8g). The sample also comprises older grains: one is concordant at ca. 600 Ma and 2 are discordant (Fig. 8g). These grains can either correspond to detrital grains (epicrysts) incorporated within the mixed tonstein (as the XRD analyses reveal a slight contamination by detrital input for this sample), or to xenocrysts from the volcanic component. The main cluster of concordant zircon analyses spreads along the concordia from ca. 310 down to ca. 270 Ma (Fig. 8h) and a concordia date cannot, therefore, be directly calculated. Among these dates, the main cluster identified by the TuffZirc algorithm, represented by 7 zircon analyses, gives a date of 290 +6/-5 Ma (Fig. 8i), while 5 older and 1 younger dates are considered as outliers. A similar concordia date of 290 ±3 Ma (not shown) can be calculated with these 7 zircon analyses. This selection of analyses to calculate a concordia date would correspond to an assumption for which the discarded older dates correspond to inherited grains. However, an alternative selection of zircon analyses corresponding to an assumption for which the younger dates have been affected by Pb loss would lead to the calculation of significantly older concordia dates.

Data obtained from 39 apatite grains are discordant and display a relatively high proportion of common lead. However, they define a linear array with an unforced lower intercept date of 289 ±12 Ma (MSWD = 1.7, Fig. 9a). If the upper intercept is anchored to a [207]Pb/[206]Pb value of 0.855 ±0.001 (calculated using the Pb evolution model of Stacey

44

and Kramers (1975) for an age of 293 ± 15Ma), the resulting lower intercept date of 295 ±4 Ma (MSWD = 1.7, Fig. 9a) is more precise although comparable within error. The weighted average ^{207}Pb-corrected date at 295 ±4 Ma (MSWD = 0.81, Fig. 9b) is also equivalent within error.

In sample LYF416.15, only 16 out of 51 zircon analyses yielded concordant dates. Discordant zircon analyses probably derive from grains that have incorporated common lead and/or have suffered Pb loss (Fig. 8j; 8h). The main cluster of concordant zircon analyses spreads between 340 and 270 Ma and therefore a concordia date cannot be calculated directly. The TuffZirc algorithm selected 11 zircon analyses to calculate a date of 298+11 –7 Ma (Fig. 8l), while 3 older and 2 younger dates are discarded. A similar concordia date at 298 ±4 Ma (Fig. 8k; MSWD = 1.16) can be calculated using 10 of these dates, and therefore discarding one younger date.

Data obtained from 28 U-Pb analyses of apatite from this sample display a high proportion of common lead. The unforced lower intercept date calculated for 27 apatite analyses (1 older analyse being considered as outlier) is 312 ±16 Ma (MSWD = 0.65, Fig. 9c). A more precise date, at 303 ±5 Ma (MSWD = 0.69, Fig. 9c) is obtained if the upper intercept is anchored at a ^{207}Pb/^{206}Pb value of 0.855 ±0.001. These two dates are equivalent within error, with the weighted average ^{207}Pb-corrected date at 307 ±8 Ma (MSWD = 0.35, Fig. 9d).

For sample LYF367.15, 52 zircon analyses were performed on zircon but only 26 yielded concordant dates (Fig. 8m, n), as discordant data show significant amount of Pb loss and variable proportions of common lead. Additionally, 6 zircon analyses that yielded older concordant dates (ranging from ca. 1200 Ma to ca. 330 Ma), suggesting, along with

45

some older discordant dates, that a population of old zircon grains is present in this sample. These old grains are interpreted to correspond to inherited or xenocryst zircon grains. Epicryst zircon grains are again considered unlikely given the almost pure volcanogenic nature of this tonstein shown by XRD analyses. The 20 other concordant dates spread between ca. 300 and ca. 250 Ma, and a concordia date can therefore not be directly calculated. The TuffZirc algorithm identify a coherent cluster of 9 out of 20 zircon analyses, yielding a TuffZirc date of 294 +2 –7 Ma. One older and 10 younger dates are considered as outliers by the TuffZirc algorithm (Fig. 8o). A poorly defined concordia date at 295 ±5 Ma (95% confidence, MSWD = 2.2) can be calculated using the 6 older concordant dates, while the remaining 14 younger zircon analyses are considered as the result of Pb loss.

Analyses performed on 25 grains of apatite are all discordant, but some display a lesser proportion of common lead than the apatite analyses from the 2 samples previously described. The unforced lower intercept date is 297 ±8 Ma (MSWD = 1.5, Fig. 9e), while the date obtained if the upper intercept is anchored at a $^{207}Pb/^{206}Pb$ value of 0.855 ±0.001 is 301 ±5 Ma (MSWD = 1.5, Fig. 9e). The weighted average ^{207}Pb-corrected date is 305 ±7 Ma (MSWD = 0.8, Fig. 9f) and is therefore similar in age with the two lower intercept dates. For this calculation, two apatite analyses that yielded older ^{207}Pb-corrected dates have been discarded.

6. Discussion

6.1. Depositional age of the continental sequence from Lucenay-lès-Aix area

Determination of depositional ages of volcaniclastic rocks from radiometric dating is not always straightforward, as recently highlighted by Rossignol et al. (2019). In order to make sure that the age obtained from radiometric dating corresponds to the deposition age, two conditions must be verified: (i) the magmatic eruption must be coeval with sedimentation (i.e., the volcanic ashes were not reworked), and (ii) the dated minerals must have crystallised shortly before the magmatic eruption. Indeed, older grains can be incorporated in volcanic ashes during the magmatic processes, as inherited grains (remaining after anatexis from the source rock), xenocrysts (incorporated into the magma from the host rock), or as antecrysts (crystallised earlier in a long-lasting magmatic chamber). While inherited grains and xenocrysts are expected to be significantly older than the volcanic eruption, antecrysts are expected to be closer in age to that of the eruption, and can be therefore sometimes more difficult to identify (e.g., Miller et al., 2007). Older grains can also be obtained when the volcanic ashes have been mixed with a variable amount of detrital components before and/or during deposition (epicrysts), which is expected to occur when the volcanic ashes are reworked. However, in such a case, a contamination should be identified from XRD analyses. Whatever the process of incorporation of older grains in the volcanic ashes, a maximum age of sedimentation can be calculated using the younger dates obtained on each sample. However, if the grains are affected by a recent, albeit small Pb loss, the $^{238}U/^{206}Pb$ ratios will increase, while the $^{207}Pb/^{206}Pb$ ratios will not change significantly, resulting in a plotting array that parallels the concordia curve. Consequently, grains that suffered this type of Pb loss will remain concordant within error but yield dates that are artificially younger than the real age of the grains (e.g., Corfu, 2013). This will in turn result in the production of a depositional age that is too young and therefore geologically meaningless.

The interpretation of depositional ages of volcanic ashes therefore mainly consists in identifying and removing analyses performed on older grains (epicrystic, inherited, xenocrystic and/or antecrystic grains) and grains affected by Pb loss. Results from U-Pb analyses on both zircon and apatite are summarised on Figure 10 and used to discuss the depositional age for each sample. The fact that samples have been selected from different stratigraphic layers on the same section, and are therefore expected to provide ages getting younger from the bottom to top, will also be used to constrain our interpretation.

The interpretation of the depositional age for samples LYF567.70 and LYF473.25 is rather straightforward. Indeed, only a few grains were either older or affected by Pb loss, and robust concordia dates, similar in age within error at ca. 299 Ma, can therefore be calculated. XRD analyses performed on these samples suggest that no contamination by detrital input occurred, the corresponding layers are interpreted to represent pyroclastic ash-fall deposits, and therefore the calculated dates can be interpreted as depositional ages. The depositional age obtained on sample LYF567.70 (299 ±2 Ma), located at the bottom of the core, provides a maximum age for the studied section, which, considering the uncertainties, cannot be older than ca. 301 Ma (at 2 σ, red line on Fig. 10), i.e., late Gzhelian (uppermost Carboniferous) or younger than 297 Ma in the case of sample LYF567.70.
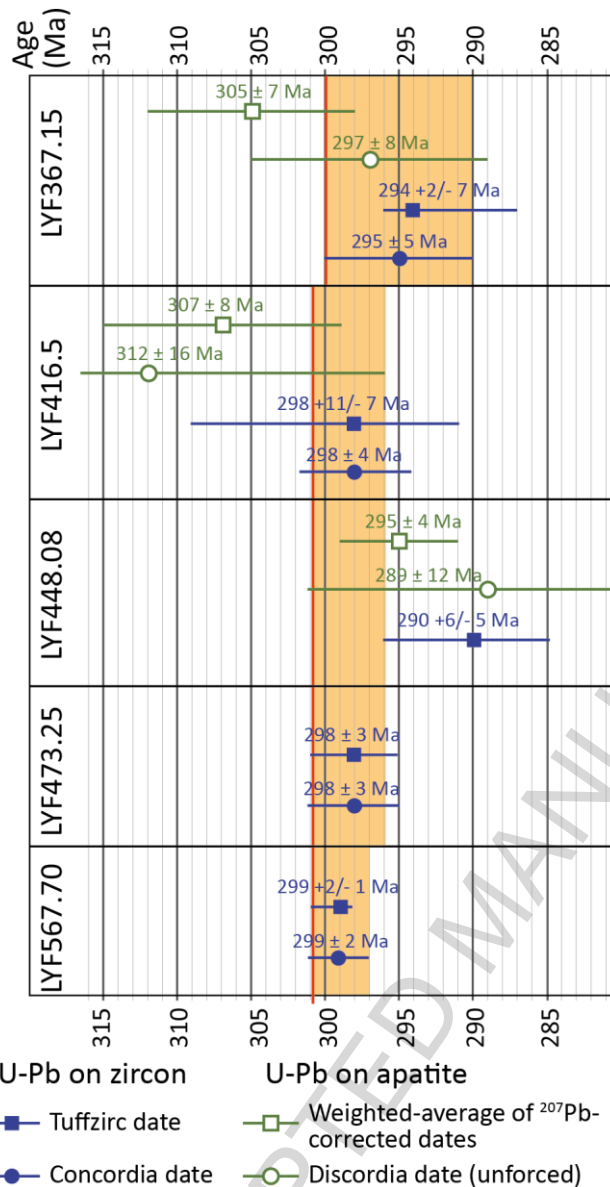
Fig. 10 Synthesis of U-Pb dating on zircon and apatite and inferred maximum (red lines) and minimum depositional ages. The depositional ages lie within the orange range.

For sample LYF448.08, the U-Pb on zircon data spread along the concordia curve and are therefore more difficult to interpret. The TuffZirc algorithm provides a median date at ca. 290 Ma calculated from the individual youngest dates. However, the dispersion of data along the concordia curve suggests that these youngest grains may have been affected by Pb loss (e.g., Spencer et al., 2016) and therefore that the depositional age might be slightly older. U-Pb zircon dates obtained for the upper (LYF416.5) and lower

49

(LYF473.25) samples are similar (298 ± 4 Ma and 298 ± 3 Ma, respectively) and therefore also constrain the depositional age of sample LYF448.08. These results confirm that the date at ca. 290 Ma obtained with the TuffZirc algorithm actually results from Pb loss. The apatite analyses for sample LYF448.08 yielded a date at 289 ± 12 Ma, comparable within error with the U-Pb zircon date. In consequence, the minimum depositional age of this sample is only based on the depositional ages obtained from the upper sample (i.e. 296 Ma, see below).

For sample LYF416.5 (Fig. 10), the concordia and TuffZirc date at c. 298 Ma obtained from U-Pb on zircon data may also be considered as questionable, due to the large dispersion of the data, although both concordia and TuffZirc ages are comparable within error. U-Pb data on apatite yielded slightly older apparent ages, which overlap within error the U-Pb dates obtained on zircon. We used the unforced discordia date to fix the minimum age of deposition for this sample (i.e., ca. 296 Ma, corresponding to 312 ± 16 Ma) although the weighted-average date is more precise. Indeed, the weighted-average date (307 ± 8 Ma) being obtained from the [207]Pb-corrected dates, calculated with a fixed (i.e., no error attached) initial [207]Pb/[206]Pb value, the calculated error could be artificially too low. Additionally, the initial [207]Pb/[206]Pb composition of the analysed apatite grains may deviate from the model from Stacey and Kramers (1975) and therefore generate slightly older dates.

At last, for sample LYF367.15, the U-Pb on zircon concordia date at ca. 295 Ma was calculated considering that the youngest analyses have been affected by Pb loss, and is consistent with the U-Pb on apatite data that yielded similar dates, within error. Both the minimum and maximum ages for the deposition of this sample are fixed by the concordia date on zircon at ca. 290 Ma and ca. 300 Ma, respectively (Fig. 10).

50

Most of the analysed samples contain a few grains significantly older than the depositional age. As XRD and geochemical analyses indicate that most of these samples correspond to pure tonsteins, these results suggest that these old dates have been mostly obtained on inherited and/or xenocrystic zircon grains incorporated in the magma. Surprisingly, sample LYF367.15 contains more grains that yielded older dates than sample LYF448.08, for which a contamination by detrital input has been identified from XRD analyses.

To summarize, combined U-Pb dating performed on both zircon and apatite allow to constrain depositional ages for the LY-F core and to discuss the part of inheritance and Pb loss recorded for several samples. Both zircon and apatite U-Pb ages are equivalent within uncertainties and range between 301 and 296 Ma (Fig. 10) for the lower part of the section (between 567.7 and 416.5 m, Figs. 2, 5), and between 300 and 290 (Fig. 10) Ma for the upper part of the section (ca. 367 m; Figs. 2, 5) which indicates that the whole sedimentary series is late Ghzelian to Sakmarian in age and probably encompass the Carboniferous-Permian boundary.

6.2. Palaeogeographic evolution

The different depositional environments defined from the sedimentological analysis of the LY-F core are now used to reconstruct the palaeo-environments in the Lucenay-lès-Aix area and their evolution through time. This study shows the predominance of lacustrine deposits, with sediment supply variations mainly preserved in delta settings. Three types of delta deposits can be distinguished.

First, deposits mainly composed of debris flows, where the detrital material (quartz, rock fragments) is mainly volcanic in origin (Fig. 4), are attributed to a volcaniclastic-rich fan delta (AF, Table 3) that would correspond to a "mixed" type delta between the alluvial-

fan delta and pyroclastic delta from Nemec (1990). Indeed, nothing in our data indicates if the volcaniclasts are juvenile or reworked, nor if these volcaniclastic deposits can be linked with the tonstein layers from this study or not.

Second, the association of delta-front, foreset and bottomset deposits (Dfr, Dfo, Dbo, Table 2), interbedded with lacustrine deposits (L1, L2, Table 2) or floodplain, characterised by swamp deposits, is considered as a Gilbert-type delta (Postma, 1990).

Third, the association of delta-front, foreset and bottomset deposits (Dfr, Dfo Table 2), evolving distally or laterally into coarse-and fine-grained debris flows within red playa-lake deposits, characterised by occurrences of hydromorphic paleosols (PL1, PL2, Table 2) is considered as a shoal-water profile delta (Postma, 1990).

From base to top, four successive palaeogeographic sketches can then be proposed (Fig. 11):

The first one (noted A, Fig. 11) displays proximal Gilbert-type delta depositional environments (Dfr, Dfo facies association, A1) associated with floodplain characterised by swamp deposits with coal layers (FP facies association, A2). This first palaeogeographic sketch corresponds to the most proximal pole of this depositional environment.

The second palaeogeographic sketch (noted B, Fig. 11) corresponds to a significantly modified landscape. Volcaniclastic-rich fan delta deposits (AF facies association, B2) are usually interbedded with lake deposits (L1, L2 facies associations, B1) or with volcanic ash and coal layers (FP facies association, B3). It is therefore assumed that (i) these debris flows were likely generated during periods of intense volcanic activity (either directly during volcanic eruptions or by reworking of volcanic deposits), and (ii) they deposited in areas where both floodplain and lake environments were previously installed during periods of quieter volcanic activity. This landscape (B, Fig. 11),

52

overall possibly characterizing a period of sustained volcanism, is particularly well recorded from 533 to 484 m.

The third palaeogeographic sketch (noted C, Fig. 11), corresponds to the distal pole of the first palaeogeographic sketch (noted A) with Gilbert-type delta deposits (Dfr, Dfo, Dbo facies association, Table 2, C1) associated with a lake environment, and a poor preservation of coal and ash layers (L1 and L2, Table 2, C2). This palaeogeographic sketch is mainly recorded from 449 to 316 m. It also corresponds to the most distal environment observed from the core data.

From depth 316 m up to the top of the core, the depositional environment is changing significantly. It is mainly characterised by playa-lake deposits (PL1, PL2, Table 2, D2) where the shoal-water profile delta is mainly characterised by delta-front facies (Dfr, Table 2, D1). It is worth mentioning that the palaeorelief depicted on the palaeographic sketch D (Fig. 11) remains unchanged, only because it remains poorly constrained by our data. However, the change in petrographic composition recorded for this part of the core may reflect a major change in source areas, and/or a reorganisation of the drainage network.

This general evolution, from base to top, shows a general evolution from a proximal delta with an episodic record of intense volcanic activity, to a more distal delta and a lacustrine environment (from A to C, Fig. 11), i.e., a major retrogradational trend, followed by a progradational trend to playa-lake environment (D, Fig. 11).
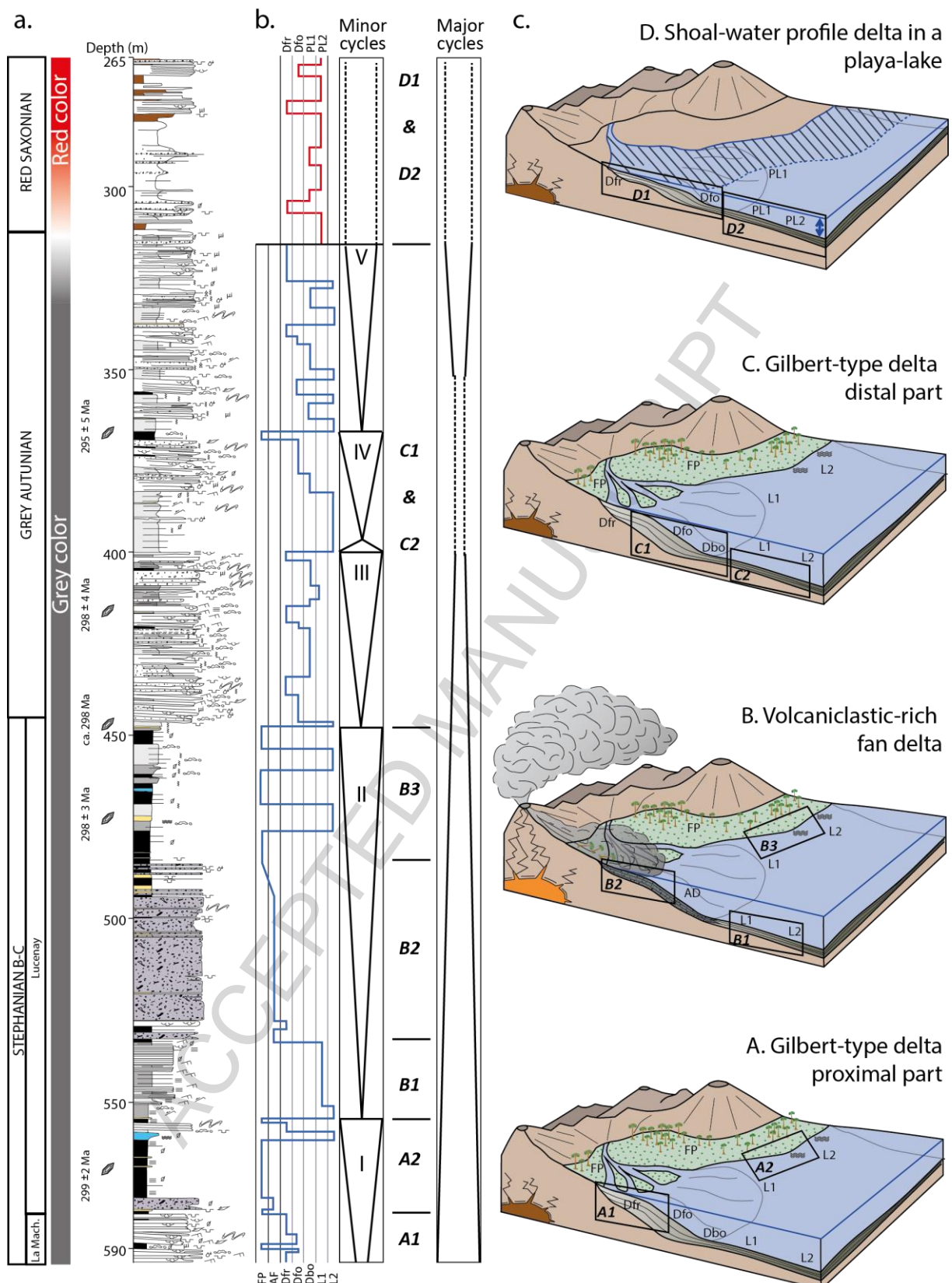
53

Fig. 11 Landscape reconstruction and evolution: a) Synthetic sedimentological log

on which are reported the U-Pb ages on zircon and the change of color of the sedimentary

series (the attribution to the different units and formations is from Donsimoni, 1990).; b) Depositional profiles and stratigraphic cycles; c) Palaeogeographical sketches (noted from A to D) on which are reported the facies associations defined in Table 3 and displayed in the depositional profiles.

6.3. Comparison with similar basins and larger scale correlations

Considering the uncertainties accompanying the U-Pb ages obtained from zircon and apatite, the deposition of the sedimentary sequence in the Lucenay-lès-Aix area took place between 301 and 290 Ma (Fig. 10), i.e., during the Late Pennsylvanian to the early Cisularian (late Gzhelian to late Sakmarian, Fig. 12). The depositional environment evolution shows a general retrogradational trend from the Stephanian B-C to the middle Grey Autunian units (Fig. 11), which corresponds to the late Gzhelian to the early Asselian (Fig. 12). The maximum flooding interval, located above sample LYF416.5, between depths 400 and 350 m (Fig. 11) could be Asselian to Sakmarian in age (Fig. 12). The progradational trend, recorded within the upper Grey Autunian and the Red Saxonian units (Fig. 11) could therefore be Sakmarian, or younger as no date has been obtained so far for the upper part of the succession.

This succession can be compared with adjacent basins for which geochronological data are available, such as the Autun and the Lodève basins (Fig. 1). By comparison with the Autun Basin (Pellenard et al., 2017), the retrogradational trend recorded by the Lucenay Fm and lower part of the Grey Autunian (Fig. 11) can be dated at the Gzhelian-Asselian transition and is therefore equivalent in age with the Igornay and Muse formations from the Autun Basin that encompass the Carboniferous/Permian boundary (Fig. 12). According to Michel et al. (2015; 2016), these formations find no equivalent in the Lodève Basin, as they record a gap of sedimentation during the late Gzhelian–late

Asselian period, while according to Bruguier et al. (2003) and Pochat and Van Den Driessche (2015), they could be equivalent with the Graissessac Fm (Fig. 12).

Fig. 12 Correlations between the Lucenay-lès-Aix area and the Autun and the Lodève basins. Here the terms "Stephanian B-C", "Grey Autunian" and "Red Saxonian" for the Lucenay area correspond to lithostratigraphic units as given in the literature (Donsimoni, 1990), not to local stratigraphic stages.

The Grey Autunian units could be, at least in part, time-equivalent in both the Lucenay-lès-Aix area and the Lodève Basin. As a consequence, the periods of maximum extension of the lacustrine environments with minor fluvial inputs, which are recorded by the Grey Autunian in the Lucenay-lès-Aix area, the Surmoullin–Millery transition in the

56

Autun Basin (Schneider et al., 2006), and the Loiras Fm in the Lodève Basin (Pochat and Van Den Driessche, 2011) could be time-equivalent in these three basins. In the Lodève Basin, as in the Lucenay-lès-Aix area, the series evolved into reddish succession within playa-lake environments.

Within the major retrogradational trend in the Lucenay-lès-Aix area, three minor cycles are recorded (noted I to III, Fig. 11). They are mainly characterised by well-expressed progradational phases, ending for the two first ones with thick coal deposits. Interbedded with these peat swamp deposits, two deltaic systems are recognised: one induced by alluvial processes only (Gilbert-type delta, sequences I and III, Fig. 11), and one induced by alluvial processes, possibly during sustained volcanic activity (volcaniclastic-rich fan delta, sequence II, Fig. 11). These minor cycles may reflect a control at the scale of the basin, or global effects. During cycle II, the volcaniclastic-rich fan delta deposits indicate a clear local input as they are expected to occur only during periods of volcanic activity. For the other cycles, only large-scale comparisons could confirm a local or a global control, such as climatic effects. For example, the peat swamp deposits, marked by coal preservation, can reflect poorly-drained conditions with a dense vegetation cover during a humid to perhumid climate, induced by high rainfalls, strongly limited erosion and sediment runoff into the stream (Cecil et al., 2014).

Overall, during the sedimentation of most of the succession, volcanism was active as shown by the well-preserved tonstein layers, and possibly the volcaniclastic fan delta deposits. The tonstein layers from the Lucenay-lès-Aix area have similar compositions than those from the Autun Basin (Pellenard et al., 2017): (i) they correspond to rhyodacite and dacite compositions (Fig. 7a); (ii) they are grouped in the calc-alkaline field (Fig. 7b) (iii) their REE patterns exhibit a marked negative Eu anomaly (Fig. 7d). The location of the volcanic centres is, however, difficult to constrain. If volcanic ashes can be transported

over long distances (up to hundreds of km for ash fall deposits), the occurrence of coarser volcaniclastic material suggests shorter transport distances. We did not prove in this study that the volcanism recorded by the volcaniclastic-rich fan deltas was contemporaneous with sedimentation and directly associated with the tuff layers (tonsteins), and no observation on the core indicates that they constitute almost unreworked proximal pyroclastic deposits. Nevertheless, they may indicate that volcanoes were active in the watershed of the basin during sedimentation. Pellenard et al. (2017) mentioned several potential volcanic sources for the tonsteins sampled in the Autun Basin, located only a few tens of kilometres away from the Lucenay-lès-Aix area. The Blisme-Montreuillon pyroclastic deposits, located in the Morvan area (Fig. 1b) are very close (< 50 km) from the depositional areas. As their ages are attributed to the late Carboniferous to Permian (Carpéna et al., 1984), they may be considered as a good candidate for the source of the volcaniclastic rocks, and possibly also of the tonstein layers in the Lucenay-lès-Aix area. However, for tonstein layers, resulting from ash fall deposits, more distal sources, such as the northern Vosges or the Black Forest may also be proposed (Pellenard et al. 2017 and references therein).

Within the retrogradational trend, we observe an evolution from Gilbert-type delta to shoal-water profile type delta (Fig. 10), attesting for an evolution toward a shallower lacustrine environment, i.e., playa-lake without coal neither ash-fall deposit preservation, and with episodic emersion. Additionally, this evolution of delta style from Gilbert-type delta to shoal-water profile type delta suggests that the depositional profile was modified and became flatter. The playa-lake environment is also characterised by an increase in the quartz content and an evolution from biotite to muscovite that could be attributed either to a change of source areas, or to a modification of the weathering conditions as muscovite is chemically more stable than biotite.

58

The general evolution, from peat swamp with coal formation to red playa-lake deposits is observed in numerous basins within the Pangean pan-tropical belt, i.e., from North America to European basins (e.g., Schneider et al., 2006; Michel et al., 2015; López-Gómez et al., 2019). The cause of this evolution is still debated by different authors that consider either a global impact induced by climate-driven changes (e.g., Montañez and Poulsen, 2013; Montañez et al., 2016) or tectonic forcing (Goddéris et al., 2017), or even a local, tectonically controlled impact (e.g., Pochat and Van Den Driessche, 2011). For instance, a local tectonic control may have affected the depositional style of the different basins. In the Lucenay-lès-Aix area, the volcanic activity induced the preservation of volcanic-rich fan delta deposits, generating a minor cycle (noted II, Fig. 11) that is not recorded in the other basins thus likely reflecting only a local control. Conversely, a major single cycle showing an evolution from a retrogradational to a progradational trend (Fig. 11) seems to have been recorded in both the Autun and Lodève basins, which were completely disconnected at this period. Although accurate age models and correlations are still lacking and would be necessary to discuss the synchronicity of this evolution, it seems reasonable to assume that this major stratigraphic cycle resulted from a same extra-basinal causes (such as an intrabelt tectonic control or a global climate change). In order to prove a climate origin, similar studies should be performed in extra-Variscan belt basins (e.g., western North American basins) to verify if a similar retrogradational / progradational evolution during the Gzelian-Asselian is recorded elsewhere. At a larger scale, the transition from organic matter-rich lake environments to red playa-lake environments are recorded in most Carboniferous to Permian European basins. Accurate age models and correlations in terrestrial Permian series are therefore necessary to discuss the synchronicity of this transition and to better constrain the origin of the long-term pan-tropical aridification.

59

7. Conclusions

The main outcome of this multidisciplinary study is to propose, for the first time, a landscape evolution of this area during the late Carboniferous to early Permian, by defining the succession of the depositional environments and the sequence stratigraphy evolution, and by providing geochronological constraints on the sedimentary deposits.

The sedimentary succession mainly records a transition from dominant lacustrine Gilbert-type delta, in which tonstein layers and volcaniclastic-rich fan delta deposits are intercalated, to playa-lake environments. The core section shows mostly prograding minor sequences and record a major retrograding / prograding trend.

In addition, maximum and minimum ages of the sedimentary section were established from U-Pb dating from both zircon and apatite for five tonstein samples collected along the LY-F core. Benefits of this coupled LA-IC-PMS U-Pb dating approach are threefold: it allows to (i) analyse a large number of grains to check the variability of zircon and apatite age populations (ii) identify and discuss Pb loss suffered by some zircon grains, and (iii) identify the autocrystic, antecrystic, inherited, xenocrystic or epiclastic nature of the dated zircon grains, by comparing the different ages obtained on zircon and apatite. The methodological approach tested in this study is easy to implement and relies on common accessory minerals in volcanic and volcaniclastic rocks. It can therefore be recommended for future geochronological studies on such rocks.

The U-Pb ages obtained on these five samples range between 301 and 296 Ma for the lower part of the section (between 567.7 and 416.5 m), and between 300 and 290 Ma for the upper part of the section (ca. 367 m). These ages are equivalent within uncertainties and indicate that the whole succession is late Ghzelian to Sakmarian in age.

At last, this study provides, for the first time, a reference section for the Carboniferous to Permian transition in this area. A major change, from organic matter-

rich lake environment to the red playa-lake environment is evidenced in the Lucenay-lès-Aix area. Our results, alone, do not allow to discriminate if this transition is controlled by global vs local effects, neither if it relates to a climatic vs a tectonic origin; further similar studies in other Carboniferous-Permian basins are therefore needed. However, our study allows to better constrain the timing of this major palaeo-environmental change, that occurred during the early Permian (Asselian – Sakmarian).

Acknowledgements

REFERENCES

Ballèvre, M., Catalán, J.R.M., López-Carmona, A., Pitra, P., Abati, J., Fernández, R.D., Ducassou, C., Arenas, R., Bosse, V., Castiñeiras, P., Fernández-Suárez, J., Barreiro, J.G., Paquette, J.-L., Peucat, J.-J., Poujol, M., Ruffet, G., Martínez, S.S., 2014. Correlation of the nappe stack in the Ibero-Armorican arc across the Bay of Biscay: a joint French–Spanish project. Geol. Soc. Lond. Spec. Publ. 405, SP405.13. https://doi.org/10.1144/SP405.13

Ballouard, C., Boulvais, P., Poujol, M., Gapais, D., Yamato, P., Tartèse, R., Cuney, M., 2015. Tectonic record, magmatic history and hydrothermal alteration in the Hercynian Guérande leucogranite, Armorican Massif, France. Lithos 220–223, 1–22. https://doi.org/10.1016/j.lithos.2015.01.027

Beccaletto, L., Capar, L., Serrano, O., Marc, S., 2015. Structural evolution and sedimentary record of the Stephano-Permian basins occurring beneath the Mesozoic sedimentary cover in the southwestern Paris basin (France). Bull. Société Géologique Fr. 186, 429–450.

Beerling, D.J., Lake, J.A., Berner, R.A., Hickey, L.J., Taylor, D.W., Royer, D.L. 2002. Carbon isotope evidence implying high O_2/CO_2 ratios in the Permo-Carboniferous atmosphere. Geochimica et Cosmochimica Acta, 66, 21, 3757–3767.

Bhattacharya, J.P., 2010. 10. Delta, in: Facies Models 4, GEOtext. Noel P. James and Robert W. Dalrymphe, pp. 233–264.

Blair, T.C., McPherson, J.G., 1994. Alluvial fan processes and forms, in: Geomorphology of Desert Environments. Springer, pp. 354–402.

Bohor, B.F., Triplehorn, D.M., 1993. Tonsteins: altered volcanic ash layers in coal-bearing sequences. Geological Society of America, 285, 44p., https://doi.org/10.1130/SPE285

Bonnion, S., Courel, L., Gelard, J.-P., Paquette, Y., 1983. L'organisation des dépôts de charbon et de stérile dans le Bassin de l'Aumance (Allier): tectonique synsédimentaire et syndiagénétique. Mém. Géologiques Univ. Dijon 8, 87–97.

Bosse, V., Feraud, G., Ruffet, G., Ballèvre, M., Peucat, J.J., De Jong, K., 2000. Late Devonian subduction and early-orogenic exhumation of eclogite-facies rocks from the Champtoceaux Complex (Variscan belt, France). Geol. J. 35, 297–325.

Bourquin, S., Guillocheau, F., Péron, S., 2009. Braided rivers within an arid alluvial plain (example from the Lower Triassic, western German Basin): recognition criteria and expression of stratigraphic cycles. Sedimentology 56, 2235–2264. https://doi.org/10.1111/j.1365-3091.2009.01078.x

Bourquin, S., Rigollet, C., Bourges, P., 1998. High-resolution sequence stratigraphy of an alluvial fan–fan delta environment: stratigraphic and geodynamic implications – An example from the Keuper Chaunoy Sandstones, Paris Basin. Sediment. Geol. 121, 207–237. https://doi.org/10.1016/S0037-0738(98)00081-5

Broutin, J., Chateauneuf, J.-J., Galtier, J., Ronchi, A., 1999. L'Autunien d'Autun reste-t-il une référence pour les dépôts continentaux du Permien inférieur d'Europe? Apport des données paléobotaniques. Géologie Fr. 17–31.

Broutin, J., Doubinger, J., Langiaux, D., Primey, D., 1986. Conséquences de la coexistence de flores à caractères stéphaniens et autuniens dans les bassins limniques d'Europe occidentale. Mémoires de la Société géologique de France, 149, 15-25.

Bruguier, O., Becq-Giraudon, J.F., Champenois, M., Deloule, E., Ludden, J., Mangin, D., 2003. Application of in situ zircon geochronology and accessory basin development during post-collisional extension: a case study from the French Massif Central. Chem. Geol. 201, 319–336.

Carpéna, J., Doubinger, J., Guérin, R., Juteau, J., Monnier, M., 1984. Le volcanisme acide de l'Ouest-Morvan dans son cadre géologique : caractérisation géochimique, structurale et chronologique de mise en place. Bull Soc Géol Fr. (7), 26, 839–859.

Cartigny, M.J.B., Ventra, D., Postma, G., van Den Berg, J.H., 2014. Morphodynamics and sedimentary structures of bedforms under supercritical-flow conditions: New insights from flume experiments. Sedimentology 61, 712–748. https://doi.org/10.1111/sed.12076

Cecil, C.B., DiMichele, W.A., Elrick, S.D., 2014. Middle and Late Pennsylvanian cyclothems, American Midcontinent: Ice-age environmental changes and terrestrial biotic dynamics. Comptes Rendus Geoscience 346, 159–168. https://doi.org/10.1016/j.crte.2014.03.008.

Chantraine, J., Autran, A., Cavelier, C., 2003. Carte géologique de la France au 1/100000. Edition révisée. Bureau de Recherches Géologiques et Minières.

Châteauneuf, J.-J., Farjanel, G., 1989. Synthèse Géologique Des Bassins Permiens Français, Mémoires du BRGM, n°128.

Chew, D.M., Petrus, J.A., Kamber, B.S., 2014. U–Pb LA–ICPMS dating using accessory mineral standards with variable common Pb. Chem. Geol. 363, 185–199. https://doi.org/10.1016/j.chemgeo.2013.11.006.

Choulet, F., Faure, M., Fabbri, O., Monié, P., 2012. Relationships between magmatism and extension along the Autun–La Serre fault system in the Variscan Belt of the eastern French Massif Central. Int. J. Earth Sci. 101, 393–413. https://doi.org/10.1007/s00531-011-0673-z.

Corfu, F., Hanchar, J.M., Hoskin, P.W., Kinny, P., 2003. Atlas of zircon textures. Rev. Mineral. Geochem. 53, 469–500.

Corfu, F., 2013. A century of U-Pb geochronology: The long quest towards concordance. Geological Society of America Bulletin 125, 33–47. https://doi.org/10.1130/B30698.1.

Courel, L., Bonnion, S., Gélard, J.P., Paquette, Y., 1989. Le bassin houiller permien de l'Aumance : bassin intramontagneux en distension sur failles réactivées, in: Dynamique et Méthodes d'étude Des Bassins Sédimentaires. Association des Sédimentologistes Français, pp. 179–195.

Davies, I.C., Walker, R.G., 1974. Transport and Deposition of Resedimented Conglomerates: The Cap Enrage Formation, Cambro-ordovician, Gaspe, Quebec. J. Sediment. Res. 44.

Debrand-Passard, S., Courbouleix, S., Lienhardt, M.- J. 1984. Synthèse géologique du Sud-Est de la France, Mémoire du BRGM, n° 125.

Delmas, J., Houel, P., Vially, R., 2002. Paris Basin, Petroleum potential (IFP regional report).

Dickinson, W.R., Gehrels, G.E., 2009. Use of U–Pb ages of detrital zircons to infer maximum depositional ages of strata: A test against a Colorado Plateau Mesozoic database. Earth Planet. Sci. Lett. 288, 115–125. https://doi.org/10.1016/j.epsl.2009.09.013.

Donsimoni, M., 2006. Le gisement de charbon de Lucenay-lès-Aix (Nièvre). Etat des connaissances acquises par le B.R.G.M. entre 1981 et 1986 - Rapport final - Projet n°PDI06CDG54 (No. BRGM/RC-54694-FR), Rapports du B.R.G.M. Orléans.

Donsimoni, M., 1990. Le gisement de charbon de Lucenay-lès-Aix (Nièvre) - Essai de synthèse géologique d'après les sondages récents (1981-1986), Editions du BRGM. ed, Documents du B.R.G.M. Orléans.

Dott, R.H.J., 1964. Wacke, Graywacke and Matrix-What Approach to Immature Sandstone Classification, J. Sediment. Res. 34, 625-632.

Ducassou, C., Poujol, M., Ruffet, G., Bruguier, O., Ballèvre, M., 2014. Relief variation and erosion of the Variscan belt: detrital geochronology of the Palaeozoic sediments from the Mauges Unit (Armorican Massif, France). Geol. Soc. Lond. Spec. Publ. 405, 137–167. https://doi.org/10.1144/SP405.6.

Echtler, H., Malavieille, J., 1990. Extensional tectonics, basement uplift and Stephano-Permian collapse basin in a late Variscan metamorphic core complex (Montagne Noire, Southern Massif Central). Tectonophysics, International IGCP Conference Project 233 177, 125–138. https://doi.org/10.1016/0040-1951(90)90277-F.

Faure, M., 1995. Late orogenic carboniferous extensions in the Variscan French Massif Central. Tectonics 14, 132–153. https://doi.org/10.1029/94TC02021.

Feys, R., Gand, G., 1983. Gisement houiller du Creusot - une tectonique de serrage dans le sillon permo-houiller de Blanzy-Creusot. Géologie Fr. 1983 (2), 97–122.

Fisher, R.V., Schmincke, H.-U., 1984. Submarine volcaniclastic rocks, in: Pyroclastic Rocks. Springer, pp. 265–296.

Franke, W., Cocks, L.R.M., Torsvik, T.H., 2017. The Palaeozoic Variscan oceans revisited. Gondwana Res. 48, 257–284. https://doi.org/10.1016/j.gr.2017.03.005.

Gand, G., 2003. Le Bassin Permien de Blanzy-Le-Creusot et ses bordures carbonifères. Bull. Inf Géol Bass Paris 40, 4–19.

Gand, G., Châteauneuf, J.-J., Durand, M., Chabard, D., Passaqui, J.-P., 2007. Permian continental environnements in the Autun basin - Pre-symposium fieldtrip guide, Association des Sédimentologistes Français, 35p.

Gapais, D., Brun, J.-P., Gumiaux, C., Cagnard, F., Ruffet, G., Le Carlier de Veslud, C., 2015. Extensional tectonics in the Hercynian Armorican belt (France). An overview. Bull. Société Géologique Fr. 186, 117–129. https://doi.org/10.2113/gssgfbull.186.2-3.117.

Genna, A., Roig, J.-Y., Debriette, P.-J., Bouchot, V., 1998. Le bassin houiller d'Argentat (Massif central français), conséquence topographique d'un plissement de son substratum varisque. Comptes Rendus Académie Sci. - Ser. IIA - Earth Planet. Sci. 327, 279–284. https://doi.org/10.1016/S1251-8050(98)80086-4.

Goddéris, Y., Donnadieu, Y., Carretier, S., Aretz, M., Dera, G., Macouin, M., Regard, V., 2017. Onset and ending of the late Palaeozoic ice age triggered by tectonically paced rock weathering. Nature Geoscience 10, 382–386. https://doi.org/10.1038/ngeo2931

Grangeon, M., Feys, R., Greber, C., Lefavrais-Raymond, 1968. Géologie profonde de la région de Decize (Nièvre). Essai de synthèse d'après les sondages récents. Bull. BRGM (2) I, 43–108.

Gulbranson, E.L., Montañez, I.P., Tabor, N.J., Oscar Limarino, C., 2015. Late Pennsylvanian aridification on the southwestern margin of Gondwana (Paganzo Basin, NW Argentina): A regional expression of a global climate perturbation. Palaeogeogr. Palaeoclimatol. Palaeoecol. 417, 220–235. https://doi.org/10.1016/j.palaeo.2014.10.029.

Heckel, P. H., Clayton, G. 2006. The Carboniferous System. Use of the new official names for the subsystems, series, and stages. Geologica acta, 4(3), 403-407.

Hong, H., Algeo, T.J., Fang, Q., Zhao, L., Ji, K., Yin, K., Wang, C., Cheng, S., 2019. Facies dependence of the mineralogy and geochemistry of altered volcanic ash beds: An example from Permian-Triassic transition strata in southwestern China. Earth-Science Reviews 190, 58–88. https://doi.org/10.1016/j.earscirev.2018.12.007

Huff, W.D. 2016. K-bentonites: A review. Am. Mineral. 101, 43–70. https://doi.org/10.2138/am-2016-5339.

Jarvis, I., Jarvis, K.E., 1985. Rare-earth element geochemistry of standard sediments: A study using inductively coupled plasma spectrometry. Chem. Geol. 53, 335–344. https://doi.org/10.1016/0009-2541(85)90078-6.

Ledru, P., Courrioux, G., Dallain, C., Lardeaux, J.M., Montel, J.M., Vanderhaeghe, O., Vitel, G., 2001. The Velay dome (French Massif Central): melt generation and granite emplacement during orogenic evolution. Tectonophysics, Partial Melting of Crust and Flow of Orogens 342, 207–237. https://doi.org/10.1016/S0040-1951(01)00165-2.

Lemirre, B., Cochelin, B., Duchene, S., de Saint Blanquat, M., Poujol, M., 2019. Origin and duration of late orogenic magmatism in the foreland of the Variscan belt (Lesponne — Chiroulet — Neouvielle area, French Pyrenees). Lithos 336-337, 183-201. https://doi.org/10.1016/j.lithos.2019.03.037

López-Gómez, J., Martín-González, F., Heredia, N., de la Horra, R., Barrenechea, J.F., Cadenas, P., Juncal, M., Diez, J.B., Borruel-Abadía, V., Pedreira, D., García-Sansegundo, J., Farias, P., Galé, C., Lago, M., Ubide, T., Fernández-Viejo, G., Gand, G., 2019. New lithostratigraphy for the Cantabrian Mountains: A common tectono-stratigraphic evolution for the onset of the Alpine cycle in the W Pyrenean realm, N Spain. Earth-Science Reviews 188, 249–271. https://doi.org/10.1016/j.earscirev.2018.11.008

Lotout, C., Pitra, P., Poujol, M., Anczkiewicz, R., Van Den Driessche, J., 2018. Timing and duration of Variscan high-pressure metamorphism in the French Massif Central: A multimethod geochronological study from the Najac Massif. Lithos 308–309, 381–394. https://doi.org/10.1016/j.lithos.2018.03.022.

Lowe, D.R., 1982. Sediment gravity flows; II, Depositional models with special reference to the deposits of high-density turbidity currents. J. Sediment. Res. 52, 279–297. https://doi.org/10.1306/212F7F31-2B24-11D7-8648000102C1865D

Ludwig, K., 2012. User's manual for Isoplot 3.75: A geochronological toolkit for Microsoft Excel: Berkeley Geochronology Center Special Publication No. 5, 75 p.

Ludwig, K.L., Mundil, R., 2002. Extracting reliable U-Pb ages and errors from complex populations of zircons from Phanerozoic tuffs, in: Goldschmidt Conference Abstracts 2002. Presented at the 12th Goldschmidt Conference, p. A463.

Ludwig, K.R., 1998. On the treatment of concordant uranium-lead ages. Geochim. Cosmochim. Acta 62, 665–676.

Malavieille, J., 1993. Late Orogenic extension in mountain belts: Insights from the basin and range and the Late Paleozoic Variscan Belt. Tectonics 12, 1115–1130. https://doi.org/10.1029/93TC01129.

Malavieille, J., Guihot, P., Costa, S., Lardeaux, J.M., Gardien, V., 1990. Collapse of the thickened Variscan crust in the French Massif Central: Mont Pilat extensional shear zone and St. Etienne Late Carboniferous basin. Tectonophysics, International IGCP Conference Project 233 177, 139–149. https://doi.org/10.1016/0040-1951(90)90278-G.

Malusà, M.G., Carter, A., Limoncelli, M., Villa, I.M., Garzanti, E., 2013. Bias in detrital zircon geochronology and thermochronometry. Chem. Geol. 359, 90–107. https://doi.org/10.1016/j.chemgeo.2013.09.016.

Marteau, P., 1983. Le Bassin Permo-Carbonifère d'Autun - Stratigraphie, sédimentologie et aspects structuraux, Editions du BRGM. ed, Documents du B.R.G.M. Orléans, 198 p.

Marteau, P., Feys, R., 1989. B6 - Le Bassin d'Autun, in: Synthèse Géologique Des Bassins Permiens Français, Mémoires Du BRGM. J.-J. Châteauneuf and G. Farjanel, Orléans, pp. 65–71.

McCann, T., 2008. The Geology of Central Europe Volume 1: Precambrian and Palaeozoic, First. ed. The Geological Society of London. https://doi.org/10.1144/CEV1P

Ménard, G., Molnar, P., 1988. Collapse of a Hercynian Tibetan Plateau into a late Palaeozoic European Basin and Range province. Nature 334, 235–237. https://doi.org/10.1038/334235a0.

Menning, M., Alekseev, A.S., Chuvashov, B.I., Davydov, V.I., Devuyst, F.X., Forke, H.C., Grunt, T.A., Hance, L., Heckel, P.H., Izokh, N.G., Jin, Y.G., Jones, P.J., Kotlyar, G.V., Kozur, H.W., Nemyrovska, T.I., Schneider, J.W., Wang, X.D., Weddige, K., Weyer, D., Jin, Y.G., 2006. Global time scale and regional stratigraphic reference scales of central and west Europe, east Europe, Tethys, south China, and North America as used in the Devonian–Carboniferous–Permian Correlation Chart 2003 (DCP 2003). Palaeogeography, Palaeoclimatology, Palaeoecology, 240, 318–372.

Miall, A.D., 1978. Lithofacies Types and Vertical Profile Models in Braided River Deposits: A Summary., in: Fluvial Sedimentology, Canadian Society of Petroleum Geologists Memoir. Miall, A.D., Calgary, pp. 597–604.

Miall, A.D., 1996. The Geology of Fluvial Deposits. Springer-Verlag Berlin Heidelberg, 582 p.

Michel, L.A., Tabor, N.J., Montañez, I.P., Schmitz, M.D., Davydov, V.I., 2015. Chronostratigraphy and Paleoclimatology of the Lodève Basin, France: Evidence for a pan-tropical aridification event across the Carboniferous–Permian boundary. Palaeogeogr. Palaeoclimatol. Palaeoecol. 430, 118–131. https://doi.org/10.1016/j.palaeo.2015.03.020.

Michel, L.A., Tabor, N.J., Montañez, I.P., Schmitz, M.D., Davydov, V.I., 2016. Reply to the comment on "Chronostratigraphy and paleoclimatology of the Lodève Basin, France: Evidence for a pan-tropical aridification event across the Carboniferous–Permian boundary" by Michel et al., (2015). Palaeogeography, Palaeoclimatology, Palaeoecology 430, 118–131. Palaeogeogr. Palaeoclimatol. Palaeoecol. 441, 1000–1004. https://doi.org/10.1016/j.palaeo.2015.10.023

Miller, J.S., Matzel, J.E.P., Miller, C.F., Burgess, S.D., Miller, R.B., 2007. Zircon growth and recycling during the assembly of large, composite arc plutons. J. Volcanol. Geotherm. Res. 167, 282–299. https://doi.org/10.1016/j.jvolgeores.2007.04.019.

Montañez, I.P., McElwain, J.C., Poulsen, C.J., White, J.D., DiMichele, W.A., Wilson, J.P., Griggs, G., Hren, M.T., 2016. Climate, p CO_2 and terrestrial carbon cycle linkages during late Palaeozoic glacial–interglacial cycles. Nat. Geosci. 9, 824–828. https://doi.org/10.1038/ngeo2822.

Montañez, I.P., Poulsen, C.J., 2013. The Late Paleozoic Ice Age: An Evolving Paradigm. Annu. Rev. Earth Planet. Sci. 41, 629–656. https://doi.org/10.1146/annurev.earth.031208.100118.

Montañez, I.P., Tabor, N.J., Niemeier, D., DiMichele, W.A., Frank, T.D., Fielding, C.R., Isbell, J.L., Birgenheier, L.P., Rygel, M.C., 2007. CO2-Forced Climate and Vegetation Instability During Late Paleozoic Deglaciation. Science 315, 87–91. https://doi.org/10.1126/science.1134207.

Moore, D.M., Reynolds, R.C., 1997. X-Ray Diffraction and the Identification and Analysis of Clay Minerals. Oxford university press, 378 p.

Mulder, T., Alexander, J., 2001. The physical character of subaqueous sedimentary density flows and their deposits. Sedimentology 48, 269–299. https://doi.org/10.1046/j.1365-3091.2001.00360.x

71

Nemchin, A.A., Cawood, P.A., 2005. Discordance of the U–Pb system in detrital zircons: Implication for provenance studies of sedimentary rocks. Sediment. Geol. 182, 143–162. https://doi.org/10.1016/j.sedgeo.2005.07.011.

Nemec, W., 1990. Deltas - remarks on terminology and classification, in: Coarse—Grained Deltas. International Association of Sedimentologists, Special Publication 10, pp. 3–12.

Opluštil, S., Jirasek, J., Schmitz, M., Matysek, D., 2017. Biotic changes around the radioisotopically constrained Carboniferous-Permian boundary in the Boskovice Basin (Czech Republic). Bull. Geosci. 92, 95–122.

Opluštil, S., Schmitz, M., Cleal, C.J., Martínek, K., 2016a. A review of the Middle–Late Pennsylvanian west European regional substages and floral biozones, and their correlation to the Geological Time Scale based on new U–Pb ages. Earth-Sci. Rev. 154, 301–335. https://doi.org/10.1016/j.earscirev.2016.01.004.

Opluštil, S., Schmitz, M., Kachlík, V., Štamberg, S., 2016b. Re-assessment of lithostratigraphy, biostratigraphy, and volcanic activity of the Late Paleozoic Intra-Sudetic, Krkonoše-Piedmont and Mnichovo Hradiště basins (Czech Republic) based on new U-Pb CA-ID-TIMS ages. Bull. Geosci., 91 (2), 399-432.

Paquette, J.-L., Ballèvre, M., Peucat, J.-J., Cornen, G., 2017. From opening to subduction of an oceanic domain constrained by LA-ICP-MS U-Pb zircon dating (Variscan belt, Southern Armorican Massif, France). Lithos 294–295, 418–437. https://doi.org/10.1016/j.lithos.2017.10.005.

Paquette, Y., 1980. Le Bassin Autunien de l'Aumance (Allier). Sédimentologie (charbon, cinérites...) - Tectonique syndiagénétique (Doctorat de 3ème cycle de Géologie). Université de Dijon, Dijon.

Paquette, Y., Feys, R., 1989. B4 - Le Bassin de Bourbon-L'Archambault (Aumance), in: Synthèse Géologique Des Bassins Permiens Français, Mémoires Du BRGM. J.-J. Châteauneuf and G. Farjanel, Orléans, pp. 43–54.

Pearce, J.A., Harris, N.B., Tindle, A.G., 1984. Trace element discrimination diagrams for the tectonic interpretation of granitic rocks. Journal of petrology 25, 956–983.

Pellenard, P., Gand, G., Schmitz, M., Galtier, J., Broutin, J., Steyer, J.-S., 2017. High-precision U-Pb zircon ages for explosive volcanism calibrating the NW European continental Autunian stratotype. Gondwana Res. 51, 118–136. https://doi.org/10.1016/j.gr.2017.07.014.

Pitra, P., Ballèvre, M., Ruffet, G., 2010. Inverted metamorphic field gradient towards a Variscan suture zone (Champtoceaux Complex, Armorican Massif, France). J. Metamorph. Geol. 28, 183–208. https://doi.org/10.1111/j.1525-1314.2009.00862.x.

Pochat, S., Van Den Driessche, J., 2011. Filling sequence in Late Paleozoic continental basins: A chimera of climate change? A new light shed given by the Graissessac–Lodève Basin (SE France). Palaeogeogr. Palaeoclimatol. Palaeoecol. 302, 170–186. https://doi.org/10.1016/j.palaeo.2011.01.006.

Pochat, S., Van Den Driessche, J., 2015. Comment on "Chronostratigraphy and Paleoclimatology of the Lodève Basin, France: Evidence for a pan-tropical aridification event across the Carboniferous–Permian boundary" by Michel, L. A., Tabor, N. J., Montañez, I. P., Schmitz, M. D., & Davydov, V. I. (2015). Palaeogeography, Palaeoclimatology, Palaeoecology, 430, 118–131 Palaeogeogr. Palaeoclimatol. Palaeoecol. 441, 997-999. https://doi.org/10.1016/j.palaeo.2015.10.024

Pochon, A., Poujol, M., Gloaguen, E., Branquet, Y., Cagnard, F., Gumiaux, C., Gapais, D., 2016. U-Pb LA-ICP-MS dating of apatite in mafic rocks: Evidence for a major magmatic event at the Devonian-Carboniferous boundary in the Armorican Massif (France). Am. Mineral. 101, 2430–2442. https://doi.org/10.2138/am-2016-5736.

Postma, G., 1990. Depositional architecture and facies of river and fan deltas: a synthesis, in: Coarse-Grained Deltas. International Association of Sedimentologists, Special Publication 10, pp. 13–27.

Postma, G., Kleverlaan, K., Cartigny, M.J.B., 2014. Recognition of cyclic steps in sandy and gravelly turbidite sequences, and consequences for the Bouma facies model. Sedimentology 61, 2268–2290. https://doi.org/10.1111/sed.12135

Postma, G., Roep, T.B., 1985. Resedimented conglomerates in the bottomsets of Gilbert-type gravel deltas. J. Sediment. Res. 55, 874–885.

Poulsen, C.J., Pollard, D., Montañez, I.P., Rowley, D. 2007. Late Paleozoic tropical climate response to Gondwanan deglaciation. Geology, 35, 9, 771–774.

Poujol, M., Pitra, P., Van den Driessche, J., Tartèse, R., Ruffet, G., Paquette, J.-L., Poilvet, J.-C., 2017. Two-stage partial melting during the Variscan extensional tectonics (Montagne Noire, France). Int. J. Earth Sci. 106, 477–500.

Primey, D., Farjanel, G., 1988. Inventaire des ressources nationales de charbon - le gisement de charbon de Lucenay-Lès-Aix (Nièvre) volume 2 - Etude paléobotanique et palynologique des gisements stéphano-autuniens de Lucenay-Lès-Aix et Devay - Bassin de Decize, Nièvre (Rapports du B.R.G.M. No. 87 SGN 652 GEO). Orléans.

Robardet, M., 2003. The Armorica "microplate": fact or fiction? Critical review of the concept and contradictory palaeobiogeogrphical data. Palaeogeogr. Palaeclimatology Palaeoecol. 195, 125–148.

74

Rossignol, C., Bourquin, S., Poujol, M., Hallot, E., Dabard, M.-P., Nalpas, T., 2016. The volcaniclastic series from the Luang Prabang Basin, Laos: A witness of a triassic magmatic arc? J. Asian Earth Sci. 120, 159–183. https://doi.org/10.1016/j.jseaes.2016.02.001.

Rossignol, C., Hallot, E., Bourquin, S., Poujol, M., Jolivet, M., Pellenard, P., Ducassou, C., Nalpas, T., Heilbronn, G., Yu, J., Dabard, M.-P., 2019. Using volcaniclastic rocks to constrain sedimentation ages: To what extent are volcanism and sedimentation synchronous? Sedimentary Geology 381, 46-64. https://doi.org/10.1016/j.sedgeo.2018.12.010

Rubi, R., Rohais, S., Bourquin, S., Moretti, I., Desaubliaux, G., 2018. Processes and typology in Gilbert-type delta bottomset deposits based on outcrop examples in the Corinth Rift. Mar. Pet. Geol. 92, 193–212. https://doi.org/10.1016/j.marpetgeo.2018.02.014.

Scheffler, K., Hoernes, S., Schwark, L. 2003. Global changes during Carboniferous–Permian glaciation of Gondwana: Linking polar and equatorial climate evolution by geochemical proxies. Geology, 31, 7, 605–608.

Schneider, J.W., Körner, F., Roscher, M., Kroner, U., 2006. Permian climate development in the northern peri-Tethys area — The Lodève Basin, French Massif Central, compared in a European and global context. Palaeogeogr. Palaeoclimatol. Palaeoecol., Evolution of the System Earth in the Late Palaeozoic: Clues from Sedimentary Geochemistry 240, 161–183. https://doi.org/10.1016/j.palaeo.2006.03.057.

Schneider, J.W., Scholze, F., Voigt, S., Götz, A.E., Opluštil, S., Ronchi, A., Bordy, E.M., Silantiev, V.V., Zharinova, V., Marchetti, L., 2017. Report on the activities of the Late Carboniferous–Permian–Early Triassic Nonmarine-Marine Correlation Working

Group for 2016 and 2017. Permophiles 65, 16–24.

Schoene, B., Bowring, S.A., 2007. Determining accurate temperature-time paths from U-Pb thermochronology: An example from the Kaapvaal cration, southern Africa. Geochimica et Cosmochimica Acta 71, 1, 165-185.

Sláma, J., Košler, J., 2012. Effects of sampling and mineral separation on accuracy of detrital zircon studies. Geochem. Geophys. Geosystems 13. https://doi.org/10.1029/2012GC004106.

Spears, D.A., 2012. The origin of tonsteins, an overview, and links with seatearths, fireclays and fragmental clay rocks. Int. J. Coal Geol., Minerals and Trace Elements in Coal 94, 22–31. https://doi.org/10.1016/j.coal.2011.09.008.

Spencer, C.J., Kirkland, C.L., Taylor, R.J.M., 2016. Strategies towards statistically robust interpretations of in situ U-Pb zircon geochronology. Geoscience Frontiers 7, 581–589. doi:10.1016/j.gsf.2015.11.006.

Stacey, J.T., Kramers, J.D., 1975. Approximation of terrestrial lead isotope evolution by a two-stage model. Earth Planet. Sci. Lett. 26, 207–221.

Tabor, N.J., DiMichele, W.A., Montañez, I.P., Chaney, D.S., 2013 Late Paleozoic continental warming of a cold tropical basin and floristic change in western Pangea. Int. J. Coal Geol., 119, 177–186

Tabor, N.J., Poulsen, C.J., 2008. Palaeoclimate across the Late Pennsylvanian–Early Permian tropical palaeolatitudes: A review of climate indicators, their distribution, and relation to palaeophysiographic climate factors. Palaeogeogr. Palaeoclimatol. Palaeoecol., The late Paleozoic Earth system 268, 293–310. https://doi.org/10.1016/j.palaeo.2008.03.052.

Tripelhorn, D.D. 1990. Applications of tonsteins to coal geology: some examples from western United States. Int. J. Coal Geol., 16, 157-160.

Vallé, B., 1986. Evolution structurale du fossé stéphano-permien de Blanzy (Massif Central, France) depuis la fin du Carbonifère: implications tectoniques régionales. Comptes Rendus Académie Sci. Sér. 2 302, 593–598.

Vallé, B., Courel, L., Gélard, J.-P., 1988. Les marqueurs de la tectonique synsédimentaire et syndiagénétique dans le bassin stéphanien à régime cisaillant de Blanzy-Montceau (Massif central, France). Bull Soc Géol Fr. 8 4, 529–540.

Van Den Driessche, J., Brun, J.P., 1991. Tectonic evolution of the Montagne Noire (Southern French Massif Central) : a model of extensional gneiss dome. Geodyn. Acta 5, 85–99.

Walker, R.G., 1975. Generalized Facies Models for Resedimented Conglomerates of Turbidite Association. GSA Bull. 86, 737–748. https://doi.org/10.1130/0016-7606(1975)86<737:GFMFRC>2.0.CO;2

Winchester, J.A., Floyd, P.A., 1977. Geochemical discrimination of different magma series and their differentiation products using immobile elements. Chem. Geol. 20, 325–343. https://doi.org/10.1016/0009-2541(77)90057-2.

Wood, D.A., 1980. The application of a Th-Hf-Ta diagram to problems of tectonomagmatic classification and to establishing the nature of crustal contamination of basaltic lavas of the British Tertiary Volcanic Province. Earth Planet. Sci. Lett. 50, 11–30. https://doi.org/10.1016/0012-821X(80)90116-8.

Zimmermann, S., Mark, C., Chew, D., Voice, P.J., 2017. Maximising data and precision from detrital zircon U-Pb analysis by LA-ICPMS: The use of core-rim ages and the single-analysis concordia age. Sediment. Geol., 375, 5-13. https://doi.org/10.1016/j.sedgeo.2017.12.020.